1 **Dynamic Response of Orthogonal 3D Woven Carbon Composites Under Soft Impact**

2 P.Turner[a,b,c], T.Liu[a,b,c]* and X.Zeng[b]

3 *[a]Centre for Structural Engineering and Informatics*
4 *[b]Composites Research Group,*
5 *[c]Department of Civil Engineering*

6 *Faculty of Engineering, The University of Nottingham,*

7 *University Park, Nottingham, NG7 2RD, U.K.*

8 **Tao.Liu@nottingham.ac.uk Tel: + 44 (0)1159 5 84059 Fax: +44 (0) 115 74 84059*

9 **Abstract**

10 This paper presents an experimental and numerical investigation into the dynamic response of 3D orthogonal

11 woven carbon composites undergoing soft impact. Composite beams of two different fibre architectures,

12 varying only by the density of through-thickness reinforcement, were centrally impacted by metallic foam

13 projectiles. Using high speed photography, the centre-point back-face deflection was measured as a function

14 of projectile impulse. Qualitative comparisons are made with a similar uni-directional laminate material. No

15 visible delamination occurred in orthogonal 3D woven samples, and beam failure was caused by tensile fibre

16 fracture at the gripped ends. This contrasts with uni-direction carbon fibre laminates, which exhibit a

17 combination of wide-spread delamination and tensile fracture. Post-impact clamped-clamped beam bending

18 tests were undertaken across the range of impact velocities tested in order to investigate any internal damage

19 within the material. Increasing impact velocity caused a reduction of beam stiffness: this phenomenon was

20 more pronounced in composites with a higher density of through-thickness reinforcement. A three-

21 dimensional finite element modelling strategy is presented and validated, showing excellent agreement with

22 the experiment in terms of back-face deflection and damage mechanisms. The numerical analyses confirm

23 negligible influence from though-thickness reinforcement in regards to back-face deflection, but significant

24 reductions in delamination damage propagation. Finite element modelling was used to demonstrate the

25 significant structural enhancements provided by the through-the-thickness weave. The contributions to the

26 field made by this research include the characterisation of 3D woven composite materials under high-speed

27 soft impact, and the demonstration of how established finite element modelling methodologies can be applied

28 to the simulation of orthogonal woven textile composite materials undergoing soft impact loading.

29 **Keywords**

30 **High speed impact, 3D woven composite, Finite element, Delamination, Material rate-dependence**

1 Introduction

The search for materials with enhanced protection against impact loading such as air blast or sand impact is of major concern in the design of military vehicles. Both rapidly expanding radial shockwaves and sand ejecta from shallow buried landmines or Improvised Explosive Devices (IEDs) can cause widespread damage of structures. There have been several experimental methodologies developed for blast-loading of structures. The first methodology was that of using explosives to load structures. This technique has the benefit of having the same loading profiles of actual dynamic loading likely to be experienced by structures, however, it adds difficulties as the wave fronts are spherical and the complex pressure signatures generated are difficult to model. Another experimental technique developed to enable the reproduction of shock waves in the laboratory, but to move away from the use of explosives, is the shock tube [1, 2]. It provides the advantage of plane wave-front generation and easily controlled experimental parameters. However, it requires large bespoke equipment, with calibration required that is unique for each shock tube system [1]. A more simplistic and economical method to load structures with a well-defined dynamic distributed impulse was introduced by Radford et al. [3], in which cylindrical metallic foam projectiles are accelerated into samples by a laboratory scale pressurised gas gun. This method has often been referred to as "soft impact" loading. The projectiles are highly compressible, exerting pressure pulses on structures in the order of 100 MPa for a duration of approximately 200 µs. The pressure pulses have characteristics remarkably similar to that observed in fluid shock loading; almost instantaneously rising pressure peaks diminishing with a rough exponential shape [3]. For a more detailed discussion of the mechanisms of blast loading, the readers are referred to Smith and Hetherington [4] for air blasts and Liu et al. [5] for sand impact.

The dynamic inertial response of a variety of monolithic and sandwich panels of composite and metal materials have been investigated via the metallic foam projectile methodology by Radford et al. [6], Radford et al. [7], McShane et al. [8] and more recently Russell et al. [9] and Kandan et al. [10]. Monolithic carbon fibre laminate beams have been shown to provide superior performance in regards to back-face deflection during dynamic shock loading than that of stainless steel beams of equal areal mass [9]. Evidence was also presented that composites with lower strength matrix can exhibit increased performance whilst undergoing dynamic soft impact loading, for both carbon fibre reinforced polymer composites and ultra-high molecular weight polyethylene (UHMWPE) composites [10]. However, laminated composites have been shown to exhibit delamination damage, even when no catastrophic longitudinal fibre fracture is observed [9]. This is a performance-limiting quality inherent within all laminate composites, and will become more exaggerated if the composite matrix strength is reduced. Delamination damage can be particularly dangerous as it is not always present during visual inspection of structures [11], and can severely reduce bending stiffness and

compressive strength [12] after impact. A more comprehensive overview of the negative effects of delamination of fibre-reinforced composites is presented by Wisnom [13].

There are various different techniques that have been developed in order to allow for enhanced protection against delamination of fibre reinforced composites, readers are referred to Tong et al. [14] for a comprehensive description of these techniques. For brevity, only three of the most prominent techniques will be mentioned here; stitching, weaving, and z-pinning. The stitching process is used extensively in industry, due to its highly automated fabrication and short set-up time. They have also been proven to have good damage-resistance properties during high intensity blast loading [15]. However, due to the inherent brittle nature of carbon and glass yarns, fibre breakages and other microstructural defects can occur during the stitching process [14]. Z-pinning is another method commonly used for improving the through-thickness properties of composite materials. This is when high strength, relatively small diameter cylindrical rods are inserted through the composite, increasing the fracture toughness and delamination resistance of the material. A comprehensive review of z-pinning is given by Mouritz [16]. Z-pinned composites have been proven to provide good protection against delamination during soft-body impact loading [17-19]. However, due to the pinning process, damage of in-plane fibres is inevitable, and reduction of in-plane properties can be quite severe. For z-pinned laminates, this can be around 27% reduction for tensile strength and at least 30% reduction for compressive strength [20].

3D orthogonal woven composites have been developed in order to address the issue of delamination damage of fibre-reinforced composite materials, without significant disturbance of the in-plane fibre architecture during the manufacturing process. 3D reinforced composites include through-the-thickness tows which wrap around the orthogonal warp and weft tows, binding them together [21]. The through-the-thickness tows provide crack bridging, and a reduction in size of continuous interfaces. This translates to a greatly improved resistance to delamination [22-25]. There have been numerous studies conducted into the ballistic impact performance of 3D woven composite materials, in particular, in the development and validation of numerical modelling strategies [26-29]. They indicate the enhanced structural performance of the 3D weave and the reduction of damage within the material. However, as of yet, there are no studies which investigate the application of the superior delamination damage resistance of 3D woven composite materials to dynamic soft impact loading. The objective of this research is to provide a comprehensive investigation into the potential of 3D woven composites to resist soft impact loading without inducing widespread damage within the material.

In this study, two different densities of orthogonal through-the-thickness reinforcement are compared via soft impact experimental testing and finite element simulation. A qualitative comparison is made with a similar UD-laminate material in regards to the damage sustained. Post-impacted beams were tested in a clamped-clamped beam bending setup in order to ascertain the development of any internal damage within the beams.

96   For numerical modelling of composite materials undergoing soft impact, inclusive of rate-dependency, the

97   constitutive and damage laws for composite materials provided by Hashin [30] and Matzenmiller et al. [31]

98   can be used to accurately predict the dynamic transient deflection of composite laminate materials undergoing

99   shock loading [32]. This paper combines this modelling strategy with explicit modelling of the through-the-

100   thickness reinforcement, allowing for a detailed examination of the exact role in which it plays during shock

101   loading. Finite element analyses compare the transient deformation and damage predictions between a 3D

102   woven composite and an equivalent UD-laminate material are made. In order to further investigate the

103   structural enhancements provided by through-the-thickness reinforcement, simulations of pre-delaminated

104   composite beams with and without though-the-thickness reinforcement are undertaken. The novelty of this

105   research is to develop understanding of orthogonal 3D woven composite beams under high-speed soft impact,

106   and the demonstration of the efficacy of a full-scale finite element modelling strategy for simulation of the

107   dynamic response of the beams.

108   The outline of the study is as follows. Section 1 presents an overview of the literature regarding the impact

109   testing of composite materials. Section 2 presents the material geometry, manufacturing technique, and quasi-

110   static material tests. Sections 3 and 4 present a description of the soft impact test methodology and finite

111   element modelling strategy, respectively. Section 5 presents a discussion of the soft impact experiment results,

112   aided with finite element predictions. Section 5 also reports the post impact clamped-clamped beam tests that

113   were conducted in order to investigate any internal damage within the composite beams. Section 6 presents a

114   summary of the main findings of the research, and states the limitations of the work.

115   2   Materials, manufacturing and quasi-static tests

116   *Materials*

117   Two 3D orthogonal woven carbon fibre reinforcements with different through-the-thickness (TTT)

118   reinforcement densities were used within this study. The first reinforcement, referred to as Full TTT, had a

119   binder-to-warp-stack ratio of 1:1 (i.e. each binder tow is separated by one vertical stack of warp tows). The

120   second reinforcement, referred to as Half TTT, had a binder-to-warp-stack-ratio of 1:2 (i.e. each binder tow is

121   separated by two vertical stacks of warp tows). Figure 1 (b) presents sketches of the two architectures. Cross

122   sectional microscopic images of the cured composite, such as the one presented in Figure 1(a), were used to

123   measure the average values for dimensions of the fibre architecture. Both materials contained an alternating

124   stack of 9 weft layers and 8 warp layers, and a cured composite thickness of 3.5 mm. Top and bottom tows

125   were orientated along the weft direction, and were the only tows with an induced crimp due to localised

126   influence of the TTT-reinforcement. As shown in Figure 1(a), the induced crimp angle was 7° from the

127   horizontal.

128   As shown in Figure 1(b), the average width and thickness of warp tows were 1.70 mm and 0.177 mm,

129   respectively. Average width and thickness of weft tow were 1.40 mm and 0.230 mm, respectively. Average

130   width and thickness of TTT-reinforcement were 0.5 mm and 0.1 mm, respectively. Spacing between TTT-

131   reinforcement was 1.74 mm in the Full TTT material and 3.48 mm in the Half TTT material. Total fibre

132   volume fraction for the Full TTT and Half TTT cured composite were 0.56 and 0.55, respectively. In order to

133   extract the material properties for tows for use in the finite element model (presented later, in Section 4), it is

134   necessary to calculate the tow volume fraction in the warp and weft directions. The tow volume fraction is

135   calculated by taking the measured total tow cross sectional area in a specific direction, and dividing into the

136   total area of the cross section. More detail of this is presented in Section 4.3. For the Full TTT material, the

137   tow volume fraction was measured as 0.285 along the warp direction, and 0.531 along the weft direction.

138   The fibre reinforcement consisted of 7 μm diameter AKSACA A-38 carbon fibre tows, with 6K filaments for

139   the warp and weft tows, and 3K filaments for the through-the-thickness reinforcement tows. The tow fibre

140   volume fractions, i.e. the ratio of the area of fibres into the area of the tow, were 0.785, 0.692, and 0.795 for

141   warp, weft, and TTT-reinforcement tows, respectively. A co-ordinate system is defined in Figure 1(b) and

142   utilised throughout this paper; the direction running parallel to the warp tows is referred to as x-direction, the

143   direction running parallel to the weft tows as y-direction, and the though-thickness direction is referred to as

144   the z-direction.

145   *Manufacturing*

146   Gurit Prime 20LV epoxy resin, with a slow hardener to resin ratio by weight of 26:100, was used. Resin

147   injection within a steel mould tool followed standard vacuum infusion methodology. The outlet port was

148   located at the centre of the tool, and four inlet ports were located at each corner. 8 bolts tightened around the

149   edge of the tool provided sufficient compaction of the dry fabric. A pressure pot was filled with compressed

150   air, with the pressure gradually increased throughout the infusion process from 0 to 6 bars. Simultaneously to

151   this, a vacuum was drawn through the outlet port at the centre of the tool in order to pull the resin through the

152   preform. To cure, the infused panel was left in an oven set at 65°C for 7 hours. The cured panel had

153   dimensions of 250 x 250 mm^2 and a thickness of 3.5 mm. Approximately 10 mm was removed from each

154   edge of the panel in order to remove any flaws due to cutting of the preform. The final cured areal density of

155   the composite material was 5300 g m^{-2} and 5210 g m^{-2} for the Full TTT and Half TTT, respectively.

156   *Quasi-static tension and compression coupon tests*

157   Quasi-static (2mm /min) uniaxial coupon tests were conducted on the Full TTT reinforcement composite

158   material in order to categorise the material response during tension and compression. Tensile experiments

159   adopted EN ISO 527-4 methodology, using dog bone shaped samples. Compression testing utilised ASTM

160   D3410/B test methods. A screw-driven Instron[©] 5581 test machine with a static 50 kN load cell was used for

161   testing. An Instron[©] 2630 clip-on extensometer was used to measure the nominal axial strain; this was

162   confirmed by a single Stingray F-146B Firewire Camera video gauge with Imentrum[©] post processing Video

163   Gauge software. The nominal stress was read directly from the load cell of the test rig. Tension and

164   compression tests for both warp and weft directions each had a minimum of five repeats.

165   Tensile and compressive tests with ±45º orientation were conducted in such a way that the warp and weft tows

166   laid at ±45º to the loading axis. Samples orientated along warp tows, weft tows, or with fibres at ±45º had a

167   width of 12 mm. Tensile tests had a length of 60 mm, compressive tests had a gauge length of 12 mm in order

168   to prevent global buckling.

169   Figure 2 (a) and (b) presents the tensile and compressive stress-strain curves of the Full TTT 3D woven

170   carbon composite material. The tensile Young's moduli were 44.4 GPa and 74.6 GPa for warp and weft

171   directions, respectively. Tensile and compressive testing along both the warp and weft directions exhibited

172   elastic-brittle fracture. Fracture of the sample was predominately governed by the fracture of the in-plane fibre

173   reinforcement. This was confirmed from scanning electron microscope (SEM) images of fracture surfaces. For

174   tensile and compressive samples orientated along the y-direction (weft), fracture occurred at the locations of

175   through-thickness reinforcement. The fracture location was attributed to stress concentrations due to the

176   crimping of the longitudinal weft tows.

177   Tension and compression tests conducted with fibres orientated at ±45º show a more ductile, yet weaker

178   response, as the tests are governed by the relatively soft matrix material. This behaviour is consistent to the

179   ductile, matrix dominated response observed for other 3D orthogonal woven carbon composites tested at ±45º

180   to the loading direction, conducted by Gerlach et al. [33].

181   Quasi-static (2mm /min) compression tests were also undertaken on the Alporas aluminium foam material that

182   was used for the projectiles in the soft impact test. The foam material exhibits a plateau at a stress of

183   approximately 2.2 MPa, corresponding to the plastic buckling of cell walls. The foam exhibits densification

184   behaviour at higher strains. The compressive stress-strain response of the aluminium foam material is

185   presented in Figure 2(c).

186   **3   Dynamic soft impact test protocol**

187   Figure 3 presents a sketch of the experimental set up for soft impact tests. Samples of width $w = 40$ mm and

188   length $L = 250$ mm were cut from the fully cured composite panels. The beams were fixed into a steel sample

189   fixture, which in turn was bolted into an aluminium alloy frame by a total of 8 M6 bolts. Clamped beams had

190   a gauge length of $l_0 = 170$ mm. The distance from the gas gun muzzle to the front edge of composite samples

191   was $s = 200$ mm. The single-stage gas-gun system developed at the University of Nottingham was used in the

192   experiment. The gas gun pressurises a 3-litre diving cylinder up to a maximum pressure of 45 bars. Pressure

193   was released via a fast-acting solenoid valve, accelerating projectiles down a 3.5 m long barrel. The barrel

194   material was hardened steel, with an outer diameter of 40 mm and a bore diameter of 28 mm. Projectiles were

195   circular cylindrical of length $l_p = 50$ mm and diameter $d_p = 27.5$ mm. Projectiles were electro-discharge

196   machined from a block of Alporas aluminium foam material of density $\rho_p = 310$ kg m^{-3}. Exit velocity of

197   projectile v_0 was measured in two ways; by two laser gates at the muzzle end of the barrel and high speed

198   photography. Exit velocity of projectiles fell within the range $160\ \text{ms}^{-1} \le v_0 \le 270\ \text{ms}^{-1}$. This corresponded

199   to a projectile momentum per unit area $I_0 = \rho_0 l_p v_0$ range of $2.48\ \text{kPa s} \le I_0 \le 4.19\ \text{kPa s}$ High speed

200   photography was employed in order to measure the back face deflection of the beams. The high speed camera

201   model Phantom Mercury HS v12.1 with a global electronic shutter was used. Typical recordings had a frame

202   rate of 22,000 fps and an exposure time of 35 μs.

203   **4   Finite Element Analysis**

204   Finite element (FE) modelling of soft impact events was utilised in order to aid interpretation of the

205   experimental tests and provide further insight into the results. The modelling strategy employed the

206   constitutive model of Matzenmiller et al. [31] and Hashin [30] for fibre composites, implemented within the

207   commercial finite element code ABAQUS. The primary aims of the numerical calculations were:

- To develop a full scale FE modelling strategy to predict the response of 3D woven composite
    materials undergoing soft impact.
- To further investigate the role of TTT-reinforcement within 3D woven composites undergoing
    dynamic soft impact.

212   *4.1   Description of the finite element model*

213   Three-dimensional (3D) finite element modelling was conducted using the explicit solver of ABAQUS

214   (Version 6.12). Each of the 17 layers of the composite beam was modelled individually, with each layer

215   composed of tows and inter-tow matrix channels. See Figure 4 for a sketch of the modelling strategy. The in-

216   plane tows, through-thickness reinforcement, and matrix channels were modelled using 4-noded quadrilateral

217   shell elements with reduced integration (S4R in ABAQUS notation), with 5 integration points through the

218   thickness. The element size of in-plane tows were approximately 1.1 mm, and the inter-tow matrix elements

219   were approximately 0.15 mm. The ABAQUS orientation assignment control was used to assign local fibre

220   orientations for individual tows. Cross sectional microscopic images, e.g. Figure 1(a), were used to acquire the

221   geometrical data such as tow/matrix sizes and locations. The surface-based cohesive contact interaction within

222   ABAQUS was employed to simulate the interaction between layers through the thickness of the beam, by

223   which delamination under dynamic impact can be simulated. The through-the-thickness reinforcement was

224   explicitly modelled, independently to the in-plane fibre architecture, with geometric parameters again taken

225   from cross-sectional microscopic images. The translational and rotational nodal degrees of freedom (DoF) of

226   the through-the-thickness reinforcement were tied to the translational and rotational nodal DoF of the in-plane

227   fibre architecture via the tie constraint option within ABAQUS. The element size of through-thickness

228   reinforcement was approximately 0.7 mm. Fixed boundary conditions were employed at the two edges of the

229   composite sample, giving a gauge length of 170 mm. All material properties, except the in-plane shear

230   stiffness of tow reinforcement, were estimated from uniaxial tension/compression coupon tests performed on

231   the composite material. The constitutive models for the tows and the matrix channels are presented in Section

232   4.2. The constitutive model for the surface-based cohesive contact interaction is presented in the Appendix to

233   this paper. The aluminium foam projectile was modelled with 8-node brick elements with reduced integration

234   (C3D8R in ABAQUS notation), using the isotropic constitutive model for metal foam described in Section

235   4.2. The "general contact" option in ABAQUS was employed to simulate the interaction between the metal

236   foam and the composite beam. A total of 210,000 shell elements were used for the composite material, and

237   14,100 solid elements for the projectile. A numerical study demonstrated that this mesh density can provide

238   converged results. All numerical simulations were conducted in 8 CPUs parallel mode using the High

239   Performance Computing (HPC) system at the University of Nottingham.

240   The numerical study included the two different material geometries used within the experimental investigation

241   i.e. Full TTT and Half TTT. In order to study the effect of the TTT reinforcement, simulations were

242   undertaken with the through-the-thickness reinforcement removed. The in-plane geometry for this model was

243   based upon that of the either the Full TTT or Half TTT material. This model is referred to as No TTT

244   throughout this paper, and is identical to non-crimp composite materials. To investigate the influence of the

245   in-plane fibre architecture, an equivalent UD-laminate material was utilised. The equivalent UD-laminate does

246   not explicitly model the geometry of each individual tow and matrix channel; the tows and matrix channels

247   are homogenised into one effective laminate, and the TTT reinforcement is removed. For clarification, Figure

248   4 (a), (b), and (c) presents sketches of the top layer of the Full TTT, No TTT, and Equivalent UD-laminate

249   material FE models, respectively.

250   ***4.2   The constitutive models employed in the FE simulations***

251   ***4.2.1   The constitutive models for each tow, TTT reinforcement and matrix channel***

252 The constitutive models of Hashin [30] and Matzenmiller et al. [31] were employed to simulate the behaviour

253 of the in-plane tows, the TTT reinforcement, and the inter-tow matrix channels during soft impact loading. As

254 indicated in Figure 4, both the tow and the matrix regions were modelled as 4-node quadrilateral shell

255 elements (S4R in ABAQUS notation). In order to describe the constitutive models, we will introduce a local

256 co-ordinate system denoted by numbers, with 11 being longitudinal to fibre direction, and 22 being transverse

257 to fibre direction. The tow and matrix elements were modelled as an orthotropic material under plane stress

258 conditions i.e. $\sigma_{33} = \sigma_{13} = \sigma_{23} = 0$. The undamaged in-plane stress strain relationship is given as;

259
$$\begin{Bmatrix} \varepsilon_{11} \\ \varepsilon_{22} \\ \gamma_{12} \end{Bmatrix} = \begin{bmatrix} 1/\overline{E}_{11} & -\overline{v}_{12}/\overline{E}_{11} & 0 \\ -\overline{v}_{21}/\overline{E}_{22} & 1/\overline{E}_{22} & 0 \\ 0 & 0 & 1/\overline{G}_{12} \end{bmatrix} \begin{Bmatrix} \sigma_{11} \\ \sigma_{22} \\ \sigma_{12} \end{Bmatrix}$$
(1)

260 where $\sigma_{ij}(i,j=1,2)$ are the in-plane stress components. ε_{11} and ε_{22} are the normal strains in the x_1 and x_2

261 directions, respectively. $\overline{E}_{11}, \overline{E}_{22}, \overline{G}_{12}, \overline{v}_{12}$ and $\overline{v}_{21}$ are longitudinal and transverse Young's modulus, shear

262 modulus, and Poisson's ratios following $\overline{v}_{21} = \left(\overline{E}_{22}/\overline{E}_{11} \right) \overline{v}_{12}$.

263 *Damage model*

264 The four primary damage modes exhibited by fibre reinforced composites (fibre rupture under tension, fibre

265 kinking and buckling under compression, matrix cracking under transverse tension and shear, and matrix

266 crushing under transverse compression and shearing) were incorporated via the anisotropic damage initiation

267 and progression models developed by Hashin [30] and Matzenmiller et al. [31]. The damage locus can be

268 defined by a stress-space, as set out by the Hashin criteria. As long as the stress state remains within the

269 damage locus, the material is classified as undamaged. Undamaged material follows the stress-strain

270 relationship defined in Equation (1). When the stress state reaches or exceeds that of the damage locus,

271 damaged is initiated, and four scalar damage variables are introduced into the stress-strain relationship. Thus,

272 the response of the material after damage initiation becomes;

273
$$\begin{Bmatrix} \varepsilon_{11} \\ \varepsilon_{22} \\ \gamma_{12} \end{Bmatrix} = \begin{Bmatrix} 1/[\overline{E}_{11}(1-d_f)] & -\overline{v}_{21}/[\overline{E}_{11}(1-d_f)] & 0 \\ -\overline{v}_{12}/[\overline{E}_{22}(1-d_m)] & 1/[\overline{E}_{22}(1-d_m)] & 0 \\ 0 & 0 & 1/[\overline{G}_{12}(1-d_s)] \end{Bmatrix} \begin{Bmatrix} \sigma_{11} \\ \sigma_{22} \\ \sigma_{12} \end{Bmatrix}$$
(2)

274 where
$$d_f = \begin{cases} d_f^t & \text{if } \sigma_{11} \geq 0 \\ d_f^c & \text{otherwise} \end{cases} \quad \text{and} \quad d_m = \begin{cases} d_m^t & \text{if } \sigma_{22} \geq 0 \\ d_m^c & \text{otherwise} \end{cases}$$
(3)

9

275 d_f^t, d_f^c, d_m^t and d_m^c are the tensile fibre, compressive fibre, tensile matrix, and compressive matrix damage

276 variables, respectively. A useful "resultant" shear damage variable, which combines all four of the damage

277 modes, is defined by

$$d_s \equiv 1 - (1 - d_f^t)(1 - d_f^c)(1 - d_m^t)(1 - d_m^c) \tag{4}$$

279 Prior to damage initiation, these four damage variables have zero values. As damage is initiated and

280 progresses within the material, these variables progress from zero up to a maximum value of unity controlled

281 by the strain of the material. The damage evolution law follows utilises a critical stress surface proposed by

282 Matzenmiller et al. [31], and is defined as;

$$\frac{\langle \sigma_{11} \rangle}{(1 - d_f^t)\overline{X}^T} \leq 1 \tag{5}$$

$$\frac{-\langle \sigma_{11} \rangle}{(1 - d_f^c)\overline{X}^C} \leq 1 \tag{6}$$

$$\left(\frac{\langle \sigma_{11} \rangle}{(1 - d_m^t)\overline{Y}} \right)^2 + \left(\frac{2\sigma_{12}}{(1 - d_s)\overline{Y}} \right)^2 \leq 1 \tag{7}$$

$$\left(\frac{\langle -\sigma_{22} \rangle}{(1 - d_m^c)\overline{\overline{Y}}} \right)^2 + \left(\frac{2\sigma_{12}}{(1 - d_s)\overline{Y}} \right)^2 \leq 1 \tag{8}$$

287 where the symbol $\langle \ \rangle$ represents the Macaulay brackets with the usual interpretation. $\overline{X}^T$ and $\overline{X}^C$ denotes the

288 longitudinal tensile and compressive strength for damage initiation. $\overline{Y}$ denotes the transverse tensile and

289 compressive strength.

290 If the current state of stress within the material exceeds the critical space defined by Equations (5) to (8), the

291 four independent damage variables (d_f^t, d_f^c, d_m^t and d_m^c) evolve and induce a linear reduction in stress with

292 increasing strain. These damage variables are continually updated following the relationship;

293
$$d_f^t = \frac{\frac{2J_f^t}{l_e \overline{X}^T}\left(\langle\varepsilon_{11}\rangle - \overline{X}^T/\overline{E}_{11}\right)}{\langle\varepsilon_{11}\rangle\left(\frac{2J_f^t}{l_e \overline{X}^T} - \overline{X}^T/\overline{E}_{11}\right)} \leq 1 \tag{9}$$

294
$$d_f^c = \frac{\frac{2J_f^c}{l_e \overline{X}^c}\left(\langle\varepsilon_{11}\rangle - \overline{X}^C/\overline{E}_{11}\right)}{\langle\varepsilon_{11}\rangle\left(\frac{2J_f^c}{l_e \overline{X}^c} - \overline{X}^C/\overline{E}_{11}\right)} \leq 1 \tag{10}$$

295
$$d_m^t = \frac{\frac{2J_m}{l_e \overline{Y}}\left(\sqrt{\langle\varepsilon_{22}\rangle^2 + \varepsilon_{12}^2} - \overline{Y}/\overline{E}_{22}\right)}{\sqrt{\langle\varepsilon_{22}\rangle^2 + \varepsilon_{12}^2}\left(\frac{2J_m}{l_e \overline{Y}} - \overline{Y}/\overline{E}_{22}\right)} \leq 1 \tag{11}$$

296
$$d_m^c = \frac{\frac{2J_m}{l_e \overline{Y}}\left(\sqrt{\langle-\varepsilon_{22}\rangle^2 + \varepsilon_{12}^2} - \overline{Y}/\overline{E}_{22}\right)}{\sqrt{\langle-\varepsilon_{22}\rangle^2 + \varepsilon_{12}^2}\left(\frac{2J_m}{l_e \overline{Y}} - \overline{Y}/\overline{E}_{22}\right)} \leq 1 \tag{12}$$

297 J_f^t, J_f^c and J_m are the tensile fibre fracture energy, compressive fibre fracture energy and matrix fracture

298 energy, respectively. In order to alleviate mesh dependency, a characteristic length scale, l_e, is utilised. The

299 matrix channels are modelled with the same constitutive law as the tows. However, for the matrix material,

300 the longitudinal and transverse properties are identical, i.e. the longitudinal fibre tensile and compressive

301 properties required in the model are taken to be the same as the material properties of the matrix.

302 *Rate dependency*

303 Numerous studies have demonstrated the importance of the strain-rate dependent behaviour of 3D woven

304 carbon fibre reinforced composites [33, 34]. Preliminary simulations of soft impact events indicated that

305 without the inclusion of rate dependency within the composite material, the predictions of the onset and

306 propagation of damage were inaccurate. In order to simulate rate dependency within the materials, a viscous

307 regularisation scheme is employed for in-plane tows, TTT reinforcement, and matrix material. A viscosity

308 coefficient, η, following Duvaunt and Lions [35], is introduced to further update each of the four previously-

309 defined damage variables (d_f^t, d_f^c, d_m^t and d_m^c). The viscous damage variables are defined as;

11

310
$$\dot{d}_i^v = \frac{1}{\eta}\left(d_i - d_i^v\right) \tag{13}$$

311 where η represents the relaxation time of the system, with d_i as the previously defined inviscid damage

312 variable, with i denoting one of the four damage modes (I through IV for d_f^t, d_f^c, d_m^t and d_m^c, respectively).

313 The term d_i^v is used to compute the damaged stiffness matrix and is updated by;

314
$$d_i^v\Big|_{t_0+\Delta t} = \frac{\Delta t}{\eta+\Delta t}\,d_i\Big|_{t_0+\Delta t} + \frac{\eta}{\eta+\Delta t}\,d_i^v\Big|_{t_0} \tag{14}$$

315 The viscous regularisation effectively slows down the rate of damage evolution, with increasing rates of

316 deformation leading to increasing fracture energies. A numerical calibration study led to the value $\eta = 5\,\mu s$.

317 This value was assumed to be identical for tension and compression for both longitudinal and transverse

318 damage modes. The viscosity coefficient employed within this study corresponds well with previously

319 calibrated values of η for carbon fibre reinforced epoxy materials, such as the one presented by Russell et al.

320 [9].

321 ### 4.2.2 Constitutive model for the metal foam projectile

322 The isotropic continuum constitutive model for metal foams developed by Deshpande and Fleck [36] was

323 used to model the Alporas aluminium foam projectiles. The von Mises effective stress, defined as

324
$$\sigma_e \equiv \sqrt{3s_{ij}s_{ij}/2} \tag{15}$$

325 with s_{ij} as the usual deviatoric stress. The yield surface for the metal foam is isotropic and follows the yield

326 function ϕ by

327
$$\phi \equiv \hat{\sigma} - Y \le 0 \tag{16}$$

328 where the equivalent stress $\hat{\sigma}$ is given by

329
$$\hat{\sigma}^2 \equiv \frac{1}{[1+(\alpha/3)^2]}\left[\sigma_e^2 + \alpha^2\sigma_m^2\right] \tag{17}$$

330   where the mean stress, $\sigma_m \equiv \sigma_{kk}/3$, and the ratio of deviatoric strength to hydrostatic strength, α, define the

331   shape of the yield surface. The right hand side of the equation is chosen so that $\hat{\sigma}$ denotes the stress

332   experienced in a uniaxial tension or compression test. The shape factor, α, can be computed using the relation

333
$$\alpha = \frac{3k}{\sqrt{9-k^2}} \text{ with } k = \frac{\sigma_c^0}{\sigma_{kk,c}^0} \tag{18}$$

334   where σ_c^0 is the initial yield stress in uniaxial compression, and $\sigma_{kk,c}^0$ is the initial yield stress in hydrostatic

335   compression.

336   Equations (16) and (17) describe an elliptical yield surface in (σ_m, σ_e) space. Y is equal to the uniaxial strength

337   in tension and compression, and the hydrostatic yield strength is equal to

338
$$\sigma_{kk} = \frac{\sqrt{1+(\alpha/3)^2}}{\alpha}Y \tag{19}$$

339   The plastic Poisson's ratio υ_p in uniaxial compression has the predicted dependence upon α

340
$$\upsilon_p = -\frac{\dot{\varepsilon}_{11}^P}{\dot{\varepsilon}_{33}^P} = \frac{(1/2)-(\alpha/3)^2}{1+(\alpha/3)^2} \tag{20}$$

341   Consistent with the quasi-static behaviour of the Alporas aluminium foam, the plastic Poisson's ratio $\upsilon_p = 0$,

342   sets the shape factor, $\alpha = 3/\sqrt{2}$. Following results from uniaxial compressive tests on the aluminium foam

343   material, presented in Figure 2, the uniaxial yield stress, σ_c, versus the true uniaxial plastic strain relationship

344   is approximated by

345
$$\sigma_c = \begin{cases} \sigma_{pl} & \hat{\varepsilon}^P \leq \varepsilon_D \\ \infty & \text{otherwise} \end{cases} \tag{21}$$

346   with the plateau strength of the foam $\sigma_{pl} = 2.2$ MPa and the true densification strain $\varepsilon_D = 1.6$. Characterisation

347   of shock wave propagation through a metallic foam is presented in Radford et al. [3]. A large stress jump is

348   seen across the shock front during progressive densification of the foam, with the width of the shock front

349   being of the order of the cell size of the material, $w \approx 5$ mm. Typical length of element during finite element

350   calculations for the metallic foam was 1.5 mm; sufficiently small enough to resolve the stress gradient.

13

4.2.3 Cohesive law for interface between layers

The surface-based cohesive contact interaction in ABAQUS was employed to simulate the interface between two adjacent layers through the thickness of the composite beam. A cohesive contact law is used to model the traction-separation behaviour within the interface between layers, allowing the simulation of delamination. If the traction stress state exceeds a critical stress state, a damage variable, $\hbar$ $(0 \leq \hbar \leq 1)$, becomes non-zero. This damage variable is a function of the fracture energy of the matrix, J_G , and used to update the traction-separation relation with a linear softening damage evolution. In compression, or the fully delaminated scenarios, the interaction between layers within the composite material is reduced to the penalty contact algorithm ("general contact" within ABAQUS), with a tangential friction coefficient of 0.3. The normal and shear stiffness of the cohesive interaction, k_n and k_s , respectively, were estimated from manufacturer's data of the epoxy resin. The maximum normal and shear traction of the cohesive interaction, t_n and t_s respectively, were estimated from the strength of the matrix material. The constitutive law for the cohesive interaction is presented in more detail in the Appendix to this paper.

4.3 Material data employed in the FE simulations

Tows and TTT reinforcement

To fully characterise the elastic response, damage initiation, and propagation of damage of the tows and TTT reinforcement, ten parameters are required. These are the longitudinal and transverse Young's moduli $\overline{E}_1$, $\overline{E}_2$, the in-plane shear modulus $\overline{G}_{12}$, in-plane Poisson's ratio $\overline{v}_{12}$, longitudinal tensile strength $\overline{X}^T$, longitudinal compressive strength $\overline{X}^C$, transverse strength $\overline{Y}$, longitudinal tensile fracture energy $\overline{J}_1^t$, longitudinal compressive fracture energy $\overline{J}_1^c$ and transverse fracture energy J_m. Simply applying the rule of mixtures to the mechanical data of carbon fibre and epoxy resin provided by the manufacturer led to an overestimation of the longitudinal stiffness and strength. This is attributed to (i) inherent fibre waviness causing a reduction of stiffness of the composite, (ii) stochastic micromechanical flaws and initial fibre misalignment causing a reduction in tensile strength, and (iii) fibre kink band formation and fibre microbuckling during compressive loading causing a reduction in compressive strength [37]. Therefore, the majority of the material properties were obtained via the rule of mixtures applied to results from quasi-static uniaxial tension and compression tests on the composite material.

Let V_{tow}^{weft} and V_{tow}^{warp} denote the volume fractions of warp tows and weft tows within the cross-section of a composite sample, respectively. They can be calculated as;

380
$$V_{tow}^{warp} = \frac{n_{warp}A_{tow}^{warp}}{A_x}, \quad V_{tow}^{weft} = \frac{n_{weft}A_{tow}^{weft}}{A_y}, \qquad (22)$$

381 where A_{tow}^{warp} and A_{tow}^{weft} denote the average transverse cross sectional areas for warp and weft tows, respectively.

382 n_{warp} and n_{weft} are the quantities of warp tows and weft tows within the composite cross-section and A_x and

383 A_y are the areas of cross sections of the composite along the x (warp) and y (weft) axis, respectively. Based

384 on the rule of mixtures we have;

385
$$\overline{E}_1 = \frac{E_x^T - (1 - V_{tow}^{warp})E_m}{V_{tow}^{warp}}, \quad \overline{v}_{12} = \frac{v_{xy} - (1 - V_{tow}^{warp})v_m}{V_{tow}^{warp}} \qquad (23)$$

386
$$\overline{X}^T = \left(\frac{E_x^T - (1 - V_{tow}^{warp})E_m}{V_{tow}^{warp}} \right) \frac{X_x^T}{E_x^T}, \quad \overline{X}^C = \left(\frac{E_x^C - (1 - V_{tow}^{warp})E_m}{V_{tow}^{warp}} \right) \frac{X_x^C}{E_x^C} \qquad (24)$$

387 For warp tows, and

388
$$\overline{E}_1 = \frac{E_y^T - (1 - V_{tow}^{weft})E_m}{V_{tow}^{weft}}, \quad \overline{v}_{12} = \frac{v_{xy} - (1 - V_{tow}^{weft})v_m}{V_{tow}^{weft}} \qquad (25)$$

389
$$\overline{X}^T = \left(\frac{E_y^T - (1 - V_{tow}^{weft})E_m}{V_{tow}^{weft}} \right) \frac{X_y^T}{E_y^T}, \quad \overline{X}^C = \left(\frac{E_y^T - (1 - V_{tow}^{weft})E_m}{V_{tow}^{weft}} \right) \frac{X_y^C}{E_y^C} \qquad (26)$$

390 for weft tows. $\{E_x^T, E_x^C, X_x^T, X_x^C\}$ and $\{E_y^T, E_y^C, X_y^T, X_y^C\}$ are the measured material tensile Young's

391 modulus, compressive Young's modulus, tensile strength and compressive strength along the x-direction

392 (warp) and y-direction (weft), respectively, v_{xy} is the measured in-plane Poisson's ratio. 0/90° uni-axial

393 tension/compression tests, described in Section 2, were used to obtain these values. Let G_{xy} represent the in-

394 plane shear modulus obtained by matrix dominated ±45° coupon tests. In Equations (24) and (26) it is

395 assumed that the strain to failure of the longitudinal tows is identical to that of the composite sample.

396 Regarding the in-plane shear modulus, $\overline{G}_{12}$, application of the rule of mixtures to mechanical test data, i.e.

397 G_{xy}, yielded a value lower than that of pure matrix. This was deemed unrealistic. It is argued that the

398 pronounced shear nonlinearity exhibited in ±45° coupon test data, i.e. Figure 2, is probably the main reason

399 that the simple rule of mixtures provides an unrealistic tow shear modulus based on coupon test data. In order

15

400   to calculate the tow shear modulus, the rule of mixtures was applied to manufacturer's data of fibre and cured

401   epoxy resin. Consider a warp or weft tow with fibre volume fraction, V_t, we have;

$$\overline{G}_{12} = \frac{G_{12f} G_m}{V_t G_m + (1 - V_t) E_m} \tag{27}$$

403   The A-38 carbon fibres of diameter 7 μm were assumed to be isotropic. In-plane shear modulus $G_{12f} = 96 \, \text{GPa}$

404   was calculated from an assumed fibre Poisson's ratio $v_f = 0.25$. The in-plane warp and weft tows each

405   contained 6000 fibres, and the TTT reinforcement contained 3000 fibres. Microscopic cross sectional images,

406   such as those presented in Figure 1(a), were used to measure the volume fractions of the warp, weft and TTT

407   reinforcement. They were measured as 0.785, 0.692 and 0.795, respectively. In the current research, as the

408   beam deflection during soft impact is normally greater than the thickness of the beam the deformation

409   mechanism within the composite material is stretch-dominated rather than bending dominated. A parameter

410   study has demonstrated that the shear modulus is not a critical parameter influencing the dynamic response of

411   the composite beam under soft impact.

412   The transverse strength of tows, $\overline{Y}$, is matrix dominated. It was determined from quasi-static uni-axial tensile

413   material coupon tests with the fibres orientated at ±45° from the loading axis. The longitudinal tensile and

414   compressive tow fracture energies, $\overline{J}_1^t$ and $\overline{J}_1^c$ were calculated using the following equations;

$$\overline{J}_1^t = 0.5 \times \frac{l_e \left(\overline{X}^T \right)^2}{\overline{E}_1} \times 1.2 \tag{28}$$

416   and

$$\overline{J}_1^c = 0.5 \times \frac{l_e \left(\overline{X}^C \right)^2}{\overline{E}_1} \times 1.2 \tag{29}$$

418   where l_e is the typical length of line across an element for a first order element, introduced in order to help

419   alleviate mesh dependency. The multiplication factor of 1.2 is incorporated in order to include the fracture

420   energy contribution from post-damage behaviour of the composites materials. It was obtained through

421   calibration against experimental measurement using detailed FE simulation on quasi-static uniaxial

422   tension/compression coupon tests [38]. The fibre volume fraction of the though-the-thickness reinforcement

423   was calculated as 0.795, and is almost identical to that of warp tows. Therefore, warp tow properties were

424   used for the TTT reinforcement. Table 1 gives a summary of all of the material properties used within the

425   finite element model for the matrix and tows.

426   *Matrix material*

427   The isotropic matrix material is characterised by six parameters i.e. Young's modulus E_m, shear modulus $\hat{G}_{12}$,

428   Poisson's ratio $\hat{v}_{12}$, normal strength σ_m, shear strength τ_m, and fracture energy J_m. The Young's modulus

429   was obtained from manufacturer's data of cured epoxy matrix $E_m = 3.5$ GPa. The matrix Poisson's ratio, $\hat{v}_{12}$,

430   and shear modulus $\hat{G}_{12}$, were also taken from manufacturer's data of cured epoxy matrix, of value 0.3 and 2

431   GPa, respectively. The longitudinal and transverse strength of the matrix material were identical and taken

432   from the quasi-static $\pm 45°$ material coupon test data presented in Figure 2. As shown in the figure, the strength

433   of the matrix material corresponds to the onset of nonlinearity of the test data, i.e. $\sigma_m = 80$ MPa. The shear

434   strength was estimated to be half that of the normal strength, i.e. $\tau_m = 40$ MPa. The transverse and

435   longitudinal tensile and compressive fracture energies were identical and also estimated from matrix

436   dominated $\pm 45°$ tension coupon tests as $J_m / l_e = 6.5$ MPa. The density of the matrix was taken from

437   manufacturer's data for cured epoxy resin, i.e. $\rho_m = 1144$ kg/m^3.

438   *Equivalent UD-laminate material*

439   It is difficult to find a UD-laminate that is equivalent to a 3D woven material for experimental testing due to

440   variations in material properties or geometry [39]. By employing the rule of mixtures to the tow and matrix

441   properties of a 3D woven composite within an FE model, it is possible to create an equivalent UD-laminate

442   material. The following material properties for the warp and weft tows within the 3D woven material model

443   are mapped into their corresponding values of an equivalent UD-laminate model, i.e. longitudinal Young's

444   modulus $\tilde{E}_1$, in-plane shear modulus $\tilde{G}_{12}$, longitudinal tensile strength $\tilde{X}^T$, longitudinal compressive strength

445    $\tilde{X}^C$, longitudinal tensile fracture energy, $\tilde{J}_1^t$, longitudinal compressive fracture energy $\tilde{J}_1^c$, and density ρ^{UD}.

446   Let the volume fraction of a tow within a warp or weft layer follow;

$$V_t^{UD} = w_t / (w_t + w_m) \tag{30}$$

448   where w_t denotes average width of tow and w_m denotes average width of inter-tow matrix channel, as shown

449   in Figure 4. Using the previously calculated values of tow Young's Modulus and strength, the effective

450   laminate properties are estimated as

17

$$\tilde{E}_1 = V_t^{UD} \overline{E}_1 + (1 - V_t^{UD}) E_m \tag{31}$$

$$\tilde{G}_{12} = \frac{\overline{G}_{12} G_m}{V_t^{UD} G_m + (1 - V_t^{UD}) \overline{G}_{12}} \tag{32}$$

$$\tilde{X}^T = V_t^{UD} \overline{X}^T + (1 - V_t^{UD}) X_m \tag{33}$$

$$\tilde{X}^C = V_t^{UD} \overline{X}^C + (1 - V_t^{UD}) X_m \tag{34}$$

$$\tilde{J}_1^t = 0.5 \times \frac{l_e (\tilde{X}^T)^2}{\tilde{E}_1} \times 1.2 \tag{35}$$

$$\tilde{J}_1^c = 0.5 \times \frac{l_e (\tilde{X}^C)^2}{\tilde{E}_1} \times 1.2 \tag{36}$$

$$\rho^{UD} = V_t^{UD} \rho^{tow} + (1 - V_t^{UD}) \rho_m \tag{37}$$

with E_m as the Young's modulus of cured epoxy resin. The modified material properties employed for the equivalent UD-laminate are presented in Table 1. A sketch of the top surface of the Equivalent UD-laminate material is presented in Figure 4(c).

5 Results and discussion

5.1 Transient deflection of beams

Soft impact experiments and FE modelling were conducted on the Full and Half TTT 3D woven composite panels orientated along the x-direction (warp) and y-direction (weft). Due to the lower fibre volume fraction in the warp direction, in comparison to the weft, the warp direction is shown to be unfavourable for resisting the loading. Figure 5 presents the measured and FE predicted normalised back-face deflections $\hat{\delta}$ of Full TTT composite beams orientated along the y-direction (weft) as a function of normalised time after moment of impact $\hat{t}$ for impulsive loading of (a) $I_0 = 2.48\ \mathrm{kPa\,s}$, (b) $I_0 = 2.64\ \mathrm{kPa\,s}$, (c) $I_0 = 3.33\ \mathrm{kPa\,s}$, and (d) $I_0 = 4.03\ \mathrm{kPa\,s}$. Also presented are FE predictions of the response of Full TTT material, No TTT material and Equivalent UD-laminate material. In order to characterise the response of the composite beams during impact, the time parameter normalised against the crush time of the projectile is used, i.e. $\hat{t} \equiv t\, v_0 / l_p$ with t as time after contact between projectile and beam, v_0 as projectile velocity, and l_p as length of projectile. In order

18

473   to remain dimensionless, a normalised deflection term $\hat{\delta} \equiv \delta / l_0$ is also used with δ as the back-face

474   deflection of the beam at centre-span and $l_0 = 170\,\text{mm}$ as the free length of the beam sample. The peak back-

475   face deflection experienced by the beam during the impact event occurs at a normalised time of approximately

476   between $1.0 \le \hat{t} \le 1.5$, with $\hat{t} = 1$ corresponding to the time at which projectile densification has completed.

477   This indicates that the transient deformation of the beam is governed primarily by the crush time of the

478   projectile.

479   FE predictions over the entire range of experimentally tested impulses show excellent fidelity in regards to the

480   peak back-face deflection exhibited by the beam during the test. The FE model also predicts the time at which

481   the peak deflection occurs during the test. The restitution of the beam occurs later than the prediction, due to

482   oscillations within the clamp during the experiment increasing the time taken for reflection of the bending

483   wave. However, the peak deflection of the beams occurred before the oscillations within the clamp, and

484   therefore had no influence from them. Figure 6(a) and (b) present the experimentally recorded and predicted

485   montages of the deformation of a Full TTT 3D woven beam orientated along the y-direction (weft)

486   undergoing an impact event of impulse $I_0 = 2.64\,\text{kPa s}$, respectively. The corresponding locations A-E

487   match with the positions highlighted in Figure 5(b). The FE prediction is shown to model accurately the

488   deformed configuration of the beam, and the crushing of the metal foam material.

489   The FE predicted back-face deflection against time response during a soft impact event for beams orientated

490   along the y-direction (weft) of the 3D woven composite material is compared to an equivalent UD-laminate

491   material in Figure 5. The Equivalent UD-laminate material exhibits the same predicted back-face deflection

492   during the soft impact event as the Full TTT material and the No TTT-reinforcement material. This result may

493   indicate that neither the TTT reinforcement nor the beam in-plane fibre architecture have significant influence

494   on the back-face deflection of composite beams undergoing soft-impact within the range of impulses tested in

495   this study. The small-scale local increases in the back-face deflection demonstrated by the UD-laminate,

496   shown in Figure 5, is attributed to delamination damage allowing relative displacement of the bottom layer

497   due to inertia. The Equivalent UD-laminate material was also predicted to exhibit a similar amount of

498   delamination damage as the No TTT reinforcement material.

499   *Effect of TTT reinforcement density on back-face deflection*

500   The Full TTT and Half TTT materials have a small variation in material areal density; 5.30 kg m^{-2} and 5.21 kg

501   m^{-2}, respectively. Therefore, to make a comparison of the response of the samples during a soft impact event,

502   the non-dimensional group suggested by Xue and Hutchinson [40] is used, which is defined as;

503
$$\bar{I}_0 = \frac{I_0}{cM} \tag{38}$$

504 where c is a characteristic wave speed, here taken to be the longitudinal wave speed of the composite material

505 $c = 7060$ ms^{-1}, and M is the areal mass of the sample. A non-dimensional peak deflection, $\bar{\delta}_{max}$, is also used,

506 and is defined as;

507
$$\bar{\delta}_{max} = \frac{\delta_{max}}{l_0} \tag{39}$$

508 where δ_{max} is the maximum back-face deflection of the sample experienced during the experiment.

509 Normalised maximum back-face deflection captured by high speed photography during experimental tests of

510 Full and Half TTT material as a function of imposed normalised impulse are plotted in Figure 7. It can be seen

511 that in this case there is no significant difference in the maximum back-face deflection between the two

512 materials tested. Also plotted is the normalised impulse at which small scale fibre fracture damage was

513 recorded on the top surface of the beams.

514 *Damage and failure of beams during soft impact*

515 Experimental tests of Half TTT orthogonal 3D woven composite material beams orientated along the x-

516 direction (warp), demonstrated the primary damage mechanism of beams undergoing a soft impact event to be

517 longitudinal fibre fracture occurring at the clamped ends. FE simulations of beams orientated along the x-

518 direction (warp) were also undertaken for two impulses, i.e. 2.95 kPa s, at which no catastrophic damage

519 occurred, and 4.19 kPa s, at which the beam failed. The normalised experimentally recorded and predicted

520 back-face deflection $\hat{\delta}$ against normalised time $\hat{t}$ after impact of two velocities of projectile for beams

521 orientated along the x-direction (warp) are presented in Figure 8. Excellent fidelity was achieved , with an

522 accurate prediction of both the back-face deflection against time and the moment of catastrophic fibre fracture

523 within the sample. To understand the failure mechanism at impulse $I_0 = 4.19\,\text{kPa s}$, Figure 9 (a) and (b)

524 presents the experimentally recorded and numerically predicted deformation of the Half TTT 3D woven

525 composite beam at selected time instants V-Z, respectively. The instants V-Z coincide with the positions

526 highlighted in Figure 8. As shown in Figure 9(b), the onset of element damage at the gripped ends

527 corresponds to the beginning of the reflection of the bending wave ($t = 264$). The sample was fully fractured at

528 the clamped ends before the reflected wave reached back to the projectile. The photographic images of the

529 fractured 3D woven composite beam after impact test and the corresponding FE numerical simulation are

530 shown in Figure 10. Both experimental results and numerical simulation demonstrated that the fracture

531 location was at the position with TTT reinforcement, which corresponds to the location with geometrical

20

532 variation in the sample. Clearly, it is the location with stress concentration. Examination of both the

533 experimental and predicted fracture surfaces reveals no visible delamination.

534 In order to compare the failure modes between the 3D woven carbon composite beam and a similar UD carbo

535 laminate beam, Figure 9(c) shows the montage of a similar UD-laminate beam under metal foam soft impact

536 with impulse $I_0 = 2.90\,\text{kPa s}$, reported by Kandan et al. [10]. The UD laminate $[(0°/90°)_7\,0°]$ had density

537 $5.21\,\text{kgm}^{-3}$, in-plane tensile Young's modulus $E_l = 85\,\text{GPa}$, tensile strength $\sigma_l^t = 980\,\text{MPa}$, and

538 compressive strength $\sigma_l^c = 630\,\text{MPa}$, which are similar to those of the 3D woven composite material

539 presented in this study. The UD-laminate beams had a thickness $t = 3.75$ mm, width $w = 35$ mm, and gauge

540 length $l_0 = 200$ mm, slightly different from the geometry of the 3D woven carbon composite beam. The UD

541 laminate material exhibited both delamination across the entire length of the beam, and catastrophic

542 longitudinal fibre fracture. An available experimental investigation [9] has also demonstrated that UD-

543 laminate composites can experience delamination at impulses lower than catastrophic beam failure. Next, we

544 will demonstrate that at impulses lower than those which caused catastrophic fibre fracture, the 3D woven

545 material exhibited no significant delamination, and only minor surface fibre fracture.

546 Beams orientated along the y-direction (weft) had a higher volume fraction that those orientated along the x-

547 direction (warp). Even the highest impulses tested within this study were not high enough to cause fibre

548 fracture of beams orientated along the y-direction (weft). After soft impact of impulse greater than

549 $I_0 \geq 3\,\text{kPa s}$, damage was observed on the front surface of the sample. Microscopic images showing the

550 surface damage of a Half TTT beam orientated along the y-direction (weft) undergoing an impact event of

551 impulse $I_0 = 3.33\,\text{kPa s}$ are presented in Figure 11(c). The damage consisted of small-scale fibre fractures

552 within the longitudinal surface tows, and was almost entirely restricted to underneath the projectile impact

553 location

554 To investigate the difference in damage mechanisms between the Full and Half TTT materials, numerical

555 predictions of Full and Half TTT material beams orientated along the y-direction (weft) impacted at an

556 impulse of $I_0 = 3.33$ kPa s were conducted. Both beams resisted delamination equally well, and there was no

557 significant difference in the tensile damage of fibres. However, there were differences in the extent of the

558 compressive damage of the surface weft tows. Figure 11(a) and (b) present the predicted compressive fibre

559 damage initiation on the top surface of beams 800 µs after projectile impact of impulse $I_0 = 3.33\,\text{kPa s}$. A

560 value of 1 indicates the onset of damage. The localised in-plane compressive fibre damage at the centre of the

561 beam corresponds well to the surface damage observed experimentally, and shown in Figure 11(c). This

562 damage is more pronounced in the Full TTT material in comparison with the Half TTT material. It is

563 suggested that the more highly constrained in-plane fibres in the Full TTT material relative to the Half TTT

564 material cause the material to undergo greater damage during impact testing. The damage was observed to be

565 concentrated at the top surface of the beam, and reduced significantly towards the centre of the beam. Next,

566 we will investigate the influence of internal damage on the bending behaviour of the beam via post-impact

567 clamped-clamped beam bending experiments.

5.2   Post impact quasi-static bending response

569   Beams orientated along the y-direction (weft) exhibited only minor visible damage during the soft impact

570   event, even up to the highest impulse of impact event. However, there still could be internal damage that could

571   reduce the structural capacity of the beam. In order to investigate this, post impact, samples of both TTT

572   reinforcement densities were tested in a quasi-static clamped-clamped beam bending test. Figure 12 presents a

573   sketch of the experimental setup for the quasi-static beam bending test. Results of the experiment are

574   compared to that of an un-impacted virgin sample. The beams were aligned along the y-direction (weft), as

575   co-ordinate system defined in Figure 1. The beams were fixed at both ends in a custom-designed clamp of

576   stainless steel, with the clamp subsequently fixed onto an I-beam. The spans of the beams between the

577   clamped ends was $L_b = 180$ mm. This free span length was purposefully chosen to be longer than the original

578   impact test beam length in order to capture damage sustained within the clamp position during soft impact

579   testing. The beams were centrally loaded by a roller across their entire width, *w*. Width of clamped beam

580   tested in this investigation was $w = 40$ mm, identical to the width of impact samples. A screw-driven Instron$^{©}$

581   5581 test machine with a static 50 kN load cell provided a constant quasi-static displacement of the roller

582   along the vertical axis (z-direction) of 5 mm/min. Roller displacement along the vertical axis, δ_b , and load

583   imposed by the roller , *P*, were measured directly from the load cell of the test rig. The stiffness was

584   calculated from between a vertical roller displacement of 2.5 mm and 7.5 mm, in order to avoid any

585   contributions from initial movement within the clamp. Figure 13 shows the load imposed by the roller, *P,*

586   against vertical roller displacement δ_b for the clamped beam test for the Full TTT material. Beams were shown

587   to retain structural integrity even after undergoing relatively high-impulse impacts $(I_0 \geq 3.0\,\text{kPa s})$. Beam

588   response was linear elastic up until a displacement $\delta_b \approx 12$ mm, when brittle fracture of in-plane

589   reinforcement tows occurred. Beam failure was attributed to fibre fracture at the centre of the samples,

590   directly under the roller position. This position is also the projectile impact location, and location of small-

591   scale fibre damage, presented in the previous section. The location of fibre fracture was the same for impacted

592   and un-impacted beams, indicating that the surface damage at this location was not the root cause for failure at

593   this position.

594   The peak load recorded during clamped beam test as a function of impact velocity is presented in Figure

595   14(a). It can be seen that there is no significant reduction in strength of beam for either the Full TTT or Half

596   TTT material even after the highest velocity of impact. The variation shown here is typical as to what is

597   expected due to stochastic flaws within the material.

598   Figure 14(b) presents the stiffness of post-impact clamped-clamped beam experiment as a function of impact

599   velocity. There is a slight reduction in stiffness during post-impact testing, with stiffness reducing linearly

with increasing impact velocity. The reduction in stiffness is seen to be greater with the Full TTT binder material relative to the Half TTT binder material. It is suggested that this is due to more highly constrained in-plane fibres in the Full TTT material cause the material to have more damage during impact testing. FE simulations presented in Section 5.3 confirm that higher TTT reinforcement density can lead to increased damage in the material.

5.3   The role of the TTT reinforcement

As demonstrated in Figure 5, the presence of the binder has no contribution to the back-face deflection of the beams. However, we will now show that there is a remarkable difference in the delamination damage sustained within the composite material. To investigate this, numerical simulations of Full and No TTT material beams orientated along the y-direction (weft) under soft impact were conducted. Figure 15(a) and (b show the predicted cohesive interaction damage contours within the beam at time $t = 700$ μs after the moment of impact for the beams with and without the TTT reinforcement, respectively. The contours shown in Figure 15 represent the value of the cohesive interaction damage variable, $\hbar$, which at a value of 1 represents fully damaged interaction between layers. $\hbar$ is defined in the Appendix to this paper. Without the presence of the TTT reinforcement, the delamination damage propagates along the entire length of the beam. Without the presence of the TTT reinforcement, the delamination damage propagates along the entire length of the beam. However, with the presence of the TTT reinforcement, the damage is notably reduced, being almost entirely restricted in location to directly under the projectile.

In order to further investigate the role of the through-the-thickness, simulations of soft impact events were undertaken with the cohesive interaction between layers removed, as shown in Figure 16. This removal of the cohesive interaction effectively simulates a fully pre-delaminated case. Inter-penetration between layers was now prevented via a penalty contact algorithm. Through this method, it is possible to simulate the material under severe conditions. It can be seen from Figure 16(a) that even with the cohesive interaction removed, the TTT reinforcement provides structural integrity to the beam, retaining its cross section throughout the test. This is juxtaposed by the predictions with both the TTT-reinforcement and cohesive interaction removed, shown in Figure 16(c), where extensive delamination is shown throughout the entire length of the beam. A transferal of momentum through the beam causes a large relative displacement of the top and bottom layers of the composite. Also presented are simulations for the case of Half TTT material (Figure 16(b)) and the equivalent UD-laminate material (Figure 16(d)). The Half TTT material exhibits a response identical to that of the Full TTT material, indicating that, in regards to the material in this study, halving the TTT reinforcement density provides no reduction in structural integrity. The Equivalent UD-laminate material behaves identically to that of the No TTT material; indicating again that in-plane reinforcement topology provides negligible influence on beam structural integrity during impulsive loading. The results presented in Figure 16 gives

24

633 indications of the superior performance of the 3D woven beams undergoing multi-hit soft impact. For
634 example, a UD-laminate beam which had previously been delaminated by a soft impact event would perform
635 far less favourably in comparison with a 3D woven composite.

636 **6   Concluding remarks**

637 An experimental investigation was undertaken in conjunction with numerical modelling in order to investigate
638 the dynamic soft impact response of two orthogonal 3D woven composite materials varying only by density of
639 through-the-thickness (TTT) reinforcement. The transient-deflection responses of the composite beams were
640 shown to be primarily governed by the projectile crush time. 3D woven composites demonstrated remarkably
641 reduced delamination damage during soft impact events in comparison with a similar UD-laminate material.
642 The failure mechanism of 3D woven composite beams was longitudinal fibre fracture at the clamped ends. At
643 impulses lower than those which caused catastrophic fibre fracture, only minor, localised fibre fracture on the
644 surface of beams was recorded. The two different densities of through-thickness reinforcement experimentally
645 tested within the study had no difference in the back-face deflection experienced during soft impact. This was
646 confirmed with the use of a finite element modelling strategy which explicitly models the geometry of the
647 through-the-thickness reinforcement. FE modelling also showed that an equivalent UD laminate material will
648 have the same maximum back-face deflection as a 3D woven material during a soft impact event, indicating
649 that the in-plane architecture has no influence on the transient deflection of beams. However, modelling of an
650 equivalent UD-laminate material did reveal greatly increased delamination damage sustained than that of the
651 3D woven material.

652 The 3D woven composite beams were shown to retain structural integrity even during high impulse soft
653 impact tests, with no delamination up to final fibre fracture. In order to investigate potential internal damage
654 within the beam clamped beam bending tests were conducted post-impact. These tests reveal negligible
655 variations in strength and only minor reductions in beam stiffness after soft impact for 3D woven material.
656 This indicates the potential for 3D woven composites to perform well during resistance of multiple soft
657 impacts. The stiffness reduction post-impact was seen to be greater with the composite containing a higher
658 density of though-thickness reinforcement. Finite element simulations of soft impact on 3D woven composites
659 of two different reinforcement densities indicated varying compressive fibre damage on the front surface of
660 the beams; demonstrating the potential for increased damage with higher densities of TTT-reinforcement.
661 Finite element predictions of pre-delaminated beams undergoing soft impact demonstrated significant
662 structural enhancement provided by the TTT-reinforcement.

663 The deterrence of delamination due to the presence of through-the-thickness reinforcement in reality has been
664 attributed to limited frictional forces between through-the-thickness reinforcement and in-plane fibre

architecture, which may not be able to prevent delamination, especially mode I dominant delamination effectively [39]. The representation of this effect via the element tie methodology is a simplification utilised in order to reduce the numerical difficulties which would arise from the explicit modelling of interactions between the through-the-thickness reinforcement and the in-plane fibre architecture. Further studies will be conducted in order to precisely classify the efficacy of the element tie methodology in regards to modelling the suppression of delamination.

The contribution provided by this research is the detailed investigation into the response of an orthogonal 3D woven carbon reinforced epoxy composite material undergoing high speed soft impact loading, and the demonstration of the efficacy of a full-scale finite element modelling strategy utilising an established continuum damage mechanics framework for the simulation of the deflection and damage modes exhibited during soft impact.

Appendix A. Cohesive interaction constitutive law

Cohesive law for interface between layers

As shown in Figure 4, there are 17 layers in the composite material. These layers are joined to neighbouring layers via a cohesive contact law. This law is used to model the traction-separation behaviour within the interface between layers, and allows the FE model to simulate inter-laminar delamination. It was at these locations that delamination damage was observed for a UD laminate composite material undergoing soft impact [10]. The undamaged elastic behaviour across the interface is governed by the following traction-separation law;

$$
\begin{Bmatrix} t_n \\ t_s \\ t_t \end{Bmatrix} = \begin{Bmatrix} k_n & 0 & 0 \\ 0 & k_s & 0 \\ 0 & 0 & k_t \end{Bmatrix} \begin{Bmatrix} \delta_n \\ \delta_s \\ \delta_t \end{Bmatrix}
\tag{40}
$$

691   where t_n, δ_n and k_n denote the normal traction, separations and stiffness, respectively; $\{t_s, t_t\}$, $\{\delta_s, \delta_t\}$ and

692    $\{k_s, k_t\}$ the two shear tractions, separations and coefficients of stiffness, respectively. The behaviour is

693   uncoupled i.e. pure normal separation does not induce cohesive forces in any of the shear directions, and pure

694   shear displacement does not induce any normal forces.

695   As with the material model for the tows and matrix, the cohesive contact consists of both a damage initiation

696   criterion and a law for the evolution of damage. If the traction stress state exists within the following surface,

697   no damage will develop;

698
$$\left[\frac{\langle t_n \rangle}{(1-\hbar)T_n}\right]^2 + \left[\frac{\langle t_s \rangle}{(1-\hbar)T_s}\right]^2 + \left[\frac{\langle t_t \rangle}{(1-\hbar)T_s}\right]^2 \leq 1 \tag{41}$$

699   Where T_n and T_s are the maximum stress states that exist in the normal and shear directions before damage

700   initiation, respectively; $\hbar\,(0 \leq \hbar \leq 1)$ denotes the damage variable for cohesive contact with $\hbar = 0$ prior to

701   damage initiation and $\hbar = 1$ at the maximum state of damage. The damage variable is defined as a function of

702   the fracture energy, J_G, following;

703
$$\hbar = \frac{\dfrac{2J_G}{t_e^0}\left(\delta_e^{\max} - \delta_e^0\right)}{\delta_e^{\max}\left(\dfrac{2J_G}{t_e^0} - \delta_e^0\right)} \leq 1 \tag{42}$$

704   where $\delta_e^{\max}$ denotes the maximum value of effective separation occurring during loading; t_e^0 and δ_e^0 are the

705   effective traction and separation at the point of damage initiation, respectively. The effective traction and

706   separation follow;

707
$$\delta_e \equiv \sqrt{\langle \delta_n \rangle^2 + \delta_s^2 + \delta_t^2} \tag{43}$$

708
$$t_e \equiv \sqrt{\langle t_n \rangle^2 + t_s^2 + t_t^2} \tag{44}$$

709   At any moment, the linear softening damage evolution law has the form;

$$
710 \qquad t_n = \begin{cases} (1-\hbar)k_n\delta_n & \text{when } \delta_n > 0 \\ k_n\delta_n & \text{otherwise} \end{cases} \qquad (45)
$$

$$
711 \qquad t_s = (1-\hbar)k_s\delta_s \qquad (46)
$$

$$
712 \qquad t_t = (1-\hbar)k_t\delta_t \qquad (47)
$$

710 When the cohesive contact is undergoing compression, i.e. when $\delta_n \leq 0$, the interaction between layers

714 governed only by a penalty contact algorithm. The "general contact" algorithm within ABAQUS was utilised,

715 with a tangential friction coefficient of 0.3.

716 An initial interface thickness of 0.1 mm was assumed. The normal and shear stiffness, k_n and k_s,

717 respectively, were estimated from manufacturer's data regarding the epoxy matrix material. The maximum

718 normal traction, t_n, was estimated from the yield stress obtained from tensile composite material tests with

719 fibres aligned at $\pm 45°$ to the loading axis, i.e. 80 MPa from Figure 2(a). The maximum shear traction, t_s, was

720 estimated as half of the maximum normal traction. The fracture energy for the cohesive interaction was

721 estimated from the area under the stress-strain curve for the $\pm 45°$ composite tensile test, i.e. $J_G = 650$ J m^{-2}.

722 This value is similar to that used within other published work, for example Shi et al. [41]. The parameters

723 used for the cohesive interaction are presented in Table 2.

724 **References**

725 [1] LeBlanc, J., Shukla, A., Rousseau, C., and Bogdanovich, A., 2007, "Shock loading of three-
726 dimensional woven composite materials," Composite Structures, 79(3), pp. 344-355.

727 [2] Tekalur, S. A., Bogdanovich, A. E., and Shukla, A., 2009, "Shock loading response of sandwich
728 panels with 3-D woven E-glass composite skins and stitched foam core," Composites Science and
729 Technology, 69(6), pp. 736-753.

730 [3] Radford, D., Deshpande, V., and Fleck, N., 2005, "The use of metal foam projectiles to simulate
731 shock loading on a structure," International Journal of Impact Engineering, 31(9), pp. 1152-1171.

732 [4] Smith, P. D., and Hetherington, J. G., 1994, Blast and ballistic loading of structures, Digital
733 Press.

734 [5] Liu, T., Fleck, N., Wadley, H., and Deshpande, V., 2013, "The impact of sand slugs against
735 beams and plates: Coupled discrete particle/finite element simulations," Journal of the Mechanics
736 and Physics of Solids, 61(8), pp. 1798-1821.

737 [6] Radford, D., Fleck, N., and Deshpande, V., 2006, "The response of clamped sandwich beams
738 subjected to shock loading," International Journal of Impact Engineering, 32(6), pp. 968-987.

739 [7] Radford, D., McShane, G., Deshpande, V., and Fleck, N., 2006, "The response of clamped
740 sandwich plates with metallic foam cores to simulated blast loading," International Journal of solids
741 and structures, 43(7), pp. 2243-2259.

742 [8] McShane, G., Radford, D., Deshpande, V., and Fleck, N., 2006, "The response of clamped
743 sandwich plates with lattice cores subjected to shock loading," European Journal of Mechanics-
744 A/Solids, 25(2), pp. 215-229.

745 [9] Russell, B., Liu, T., Fleck, N., and Deshpande, V., 2012, "The soft impact of composite sandwich
746 beams with a square-honeycomb core," International Journal of Impact Engineering, 48, pp. 65-81.

747 [10] Kandan, K., Russell, B. P., Fleck, N. A., O'Masta, M., Wadley, H. N. G., and Deshpande, V. S.,
748 2013, "The soft impact response of composite laminate beams," International Journal of Impact
749 Engineering, 60(0), pp. 24-36.

750 [11] Shyr, T.-W., and Pan, Y.-H., 2003, "Impact resistance and damage characteristics of composite
751 laminates," Composite Structures, 62(2), pp. 193-203.

752 [12] Cantwell, W., and Morton, J., 1991, "The impact resistance of composite materials—a review,"
753 composites, 22(5), pp. 347-362.

754 [13] Wisnom, M., 2012, "The role of delamination in failure of fibre-reinforced composites,"
755 Philosophical Transactions of the Royal Society of London A: Mathematical, Physical and
756 Engineering Sciences, 370(1965), pp. 1850-1870.

757 [14] Tong, L., Mouritz, A. P., and Bannister, M., 2002, 3D fibre reinforced polymer composites,
758 Elsevier.

759 [15] Mouritz, A., 2001, "Ballistic impact and explosive blast resistance of stitched composites,"
760 Composites Part B: Engineering, 32(5), pp. 431-439.

761 [16] Mouritz, A., 2007, "Review of z-pinned composite laminates," Composites Part A: applied
762 science and manufacturing, 38(12), pp. 2383-2397.

763 [17] Kalwak, G., and Jevons, M., 2012, "Experimental assessment and design of through thickness
764 reinforcement in thick composite laminates subjected to bird strike loading," Proceedings of ECCM
765 15 Conference, 2012.

766 [18] Kalwak, G., Read, S., Jevons, M., and Petrinic, N., 2014, "Investigation of the delamination
767 characteristics of composite specimens with through thickness reinforcement using an inertia
768 constrained soft body beam bend test specimens," ECC16 conference proceedings.

769 [19] Mohamed, G., Kalwak, G., Hallett, S. R., and Jevons, M., 2014, "Modelling soft body impact of
770 through-thickness reinforcement composites," ECCM16.

[20] Steeves, C. A., and Fleck, N. A., 2006, "In-plane properties of composite laminates with through-thickness pin reinforcement," International Journal of solids and structures, 43(10), pp. 3197-3212.

[21] Bogdanovich, A., and Mohamed, M., 2009, "Three-dimensional reinforcements for composites," SAMPE journal, 45(6), pp. 8-28.

[22] Barrett, D. J., 1996, "The mechanics of z-fiber reinforcement," Composite Structures, 36(1), pp. 23-32.

[23] Grassi, M., and Zhang, X., 2003, "Finite element analyses of mode I interlaminar delamination in z-fibre reinforced composite laminates," Composites Science and Technology, 63(12), pp. 1815-1832.

[24] Bahei-El-Din, Y. A., and Zikry, M. A., 2003, "Impact-induced deformation fields in 2D and 3D woven composites," Composites Science and Technology, 63(7), pp. 923-942.

[25] Grogan, J., Tekalur, S. A., Shukla, A., Bogdanovich, A., and Coffelt, R. A., 2007, "Ballistic resistance of 2D and 3D woven sandwich composites," Journal of Sandwich Structures and Materials, 9(3), pp. 283-302.

[26] Yu, Y., Wang, X., and Lim, C., 2009, "Ballistic impact of 3D orthogonal woven composite by a spherical bullet: experimental study and numerical simulation," International Journal of Engineering and Applied Sciences, 1, pp. 11-18.

[27] Li, Z., Sun, B., and Gu, B., 2010, "FEM simulation of 3D angle-interlock woven composite under ballistic impact from unit cell approach," Computational Materials Science, 49(1), pp. 171-183.

[28] Ghosh, R., and De, S., 2014, "Z-fiber influence on high speed penetration of 3D orthogonal woven fiber composites," Mechanics of materials, 68, pp. 147-163.

[29] Jia, X., Sun, B., and Gu, B., 2011, "A numerical simulation on ballistic penetration damage of 3D orthogonal woven fabric at microstructure level," International Journal of Damage Mechanics, p. 1056789510397078.

[30] Hashin, Z., 1980, "Failure criteria for unidirectional fiber composites," Journal of applied mechanics, 47(2), pp. 329-334.

[31] Matzenmiller, A., Lubliner, J., and Taylor, R., 1995, "A constitutive model for anisotropic damage in fiber-composites," Mechanics of materials, 20(2), pp. 125-152.

[32] Russell, B., Malcom, A., Wadley, H., and Deshpande, V., 2010, "Dynamic compressive response of composite corrugated cores," Journal of mechanics of materials and structures, 5(3), pp. 477-493.

[33] Gerlach, R., Siviour, C. R., Wiegand, J., and Petrinic, N., 2012, "In-plane and through-thickness properties, failure modes, damage and delamination in 3D woven carbon fibre composites subjected to impact loading," Composites Science and Technology, 72(3), pp. 397-411.

807 [34] Pankow, M., Salvi, A., Waas, A., Yen, C., and Ghiorse, S., 2011, "Split Hopkinson pressure bar
808 testing of 3D woven composites," Composites Science and Technology, 71(9), pp. 1196-1208.

809 [35] Duvaunt, G., and Lions, J., 1976, Inequalities in Mechanics and Physics, Springer.

810 [36] Deshpande, V., and Fleck, N., 2000, "High strain rate compressive behaviour of aluminium
811 alloy foams," International Journal of Impact Engineering, 24(3), pp. 277-298.

812 [37] Cox, B., Dadkhah, M., Inman, R., Morris, W., and Zupon, J., 1992, "Mechanisms of
813 compressive failure in 3D composites," Acta Metallurgica et Materialia, 40(12), pp. 3285-3298.

814 [38] Turner, P., Liu, T., and Zeng, X., 2015, "Collapse of 3D orthogonal woven carbon fibre
815 composites under in-plane tension, compression, and out-of-plane bending," (Under review).

816 [39] Mouritz, A., and Cox, B., 2010, "A mechanistic interpretation of the comparative in-plane
817 mechanical properties of 3D woven, stitched and pinned composites," Composites Part A: applied
818 science and manufacturing, 41(6), pp. 709-728.

819 [40] Xue, Z., and Hutchinson, J. W., 2004, "A comparative study of impulse-resistant metal
820 sandwich plates," International Journal of Impact Engineering, 30(10), pp. 1283-1305.

821 [41] Shi, Y., Swait, T., and Soutis, C., 2012, "Modelling damage evolution in composite laminates
822 subjected to low velocity impact," Composite Structures, 94(9), pp. 2902-2913.

823

824 Table 1: Material properties for matrix, warp, weft, and TTT reinforcement tows used within the finite
825 element model

Material	Property	Value
Matrix	Density (kg m^{-3})	1144
	E_m (GPa)	3.5
	$\hat{G}_{12}$ (GPa)	2.0
	$\hat{v}_{12}$	0.3
	σ_m (MPa)	80
	τ_m (MPa)	40
	J_m/l_e (MPa)	6.5
Warp Tow / TTT Reinforcement	Density (kg m^{-3})	1628
	$\overline{E}_1$ (GPa)	146.8
	$\overline{E}_2$ (GPa)	3.5
	$\overline{v}_{12}$	0.25
	$\overline{G}_{12},\ \overline{G}_{13},\ \overline{G}_{23}$ (GPa)	14.37
	$\overline{X}^T$ (MPa)	2020
	$\overline{X}^C$ (MPa)	1610

	$\overline{Y}$ (MPa)	80
	$\overline{X}^s$, $\overline{Y}^s$ (MPa)	40
	$\overline{J}_1^t/l_e$ (MPa)	16.68
	$\overline{J}_1^c/l_e$ (MPa)	10.60
	J_m/l_e (MPa)	6.5
Weft Tow	Density (kg m^{-3})	1570
	$\overline{E}_1$ (GPa)	135.7
	$\overline{E}_2$ (GPa)	3.5
	$\overline{\nu}_{12}$	0.25
	$\overline{G}_{12}$, $\overline{G}_{13}$, $\overline{G}_{23}$ (GPa)	7.16
	$\overline{X}^T$ (MPa)	1720
	$\overline{X}^C$ (MPa)	1110
	$\overline{Y}$ (MPa)	80
	$\overline{X}^s$, $\overline{Y}^s$ (MPa)	40
	$\overline{J}_1^t/l_e$ (MPa)	13.08
	$\overline{J}_1^c/l_e$ (MPa)	5.45
	J_m/l_e (MPa)	6.5
Equivalent UD-laminate Warp (Modified values)	Density (kg m^{-3})	1525
	$\tilde{E}_1$ (GPa)	122.2
	$\tilde{G}_{12}$ (GPa)	5.78
	$\tilde{X}^T$ (MPa)	1590
	$\tilde{X}^C$ (MPa)	1280
	$\tilde{J}_1^t$ (MPa)	12.41
	$\tilde{J}_1^c$ (MPa)	8.04
Equivalent UD-laminate Weft (Modified values)	Density (kg m^{-3})	1530
	$\tilde{E}_1$ (GPa)	126.4
	$\tilde{G}_{12}$ (GPa)	4.93
	$\tilde{X}^T$ (MPa)	1590
	$\tilde{X}^C$ (MPa)	1040
	$\tilde{J}_1^t$ (MPa)	12.00
	$\tilde{J}_1^c$ (MPa)	5.13

826

827   Table 2: Material parameters for cohesive contact used to simulate delamination between layers of 3D woven

828   composite material

Property	Value
k_n	3.5 GPa mm^{-1}
k_s, k_t	2.0 GPa mm^{-1}
t_n	80 MPa
t_s, t_t	40 MPa
J_G	650 J m^{-2}

(a)

(b)
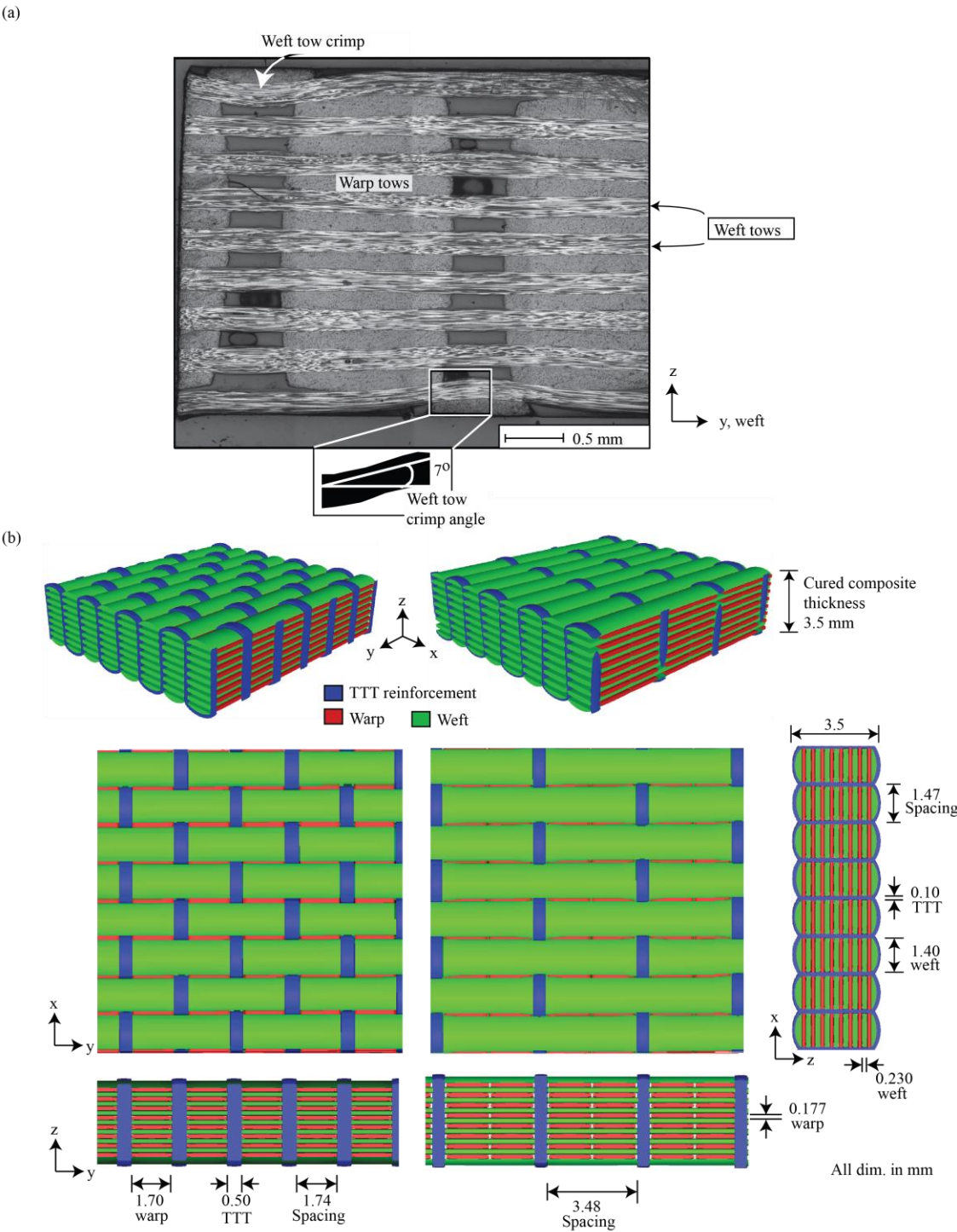
831   Figure 1.(a) Microscopic image of the composite cross-section along the weft direction, with crimping of the

832   weft tows due to the presence of the TTT reinforcement. (b) Sketch of 3D orthogonal woven carbon

833   composites showing Full through-the-thickness (TTT) reinforcement with the binder-to-warp-stack ratio of

834   1:1 on the left and Half TTT reinforcement with the binder-to-warp-stack ratio of 1:2 on the right, with the

835   dimensions as the average measurements of the cured composites. (For interpretation of the colour legend in

836   this figure, the reader is referred to the web version of this article.)

837
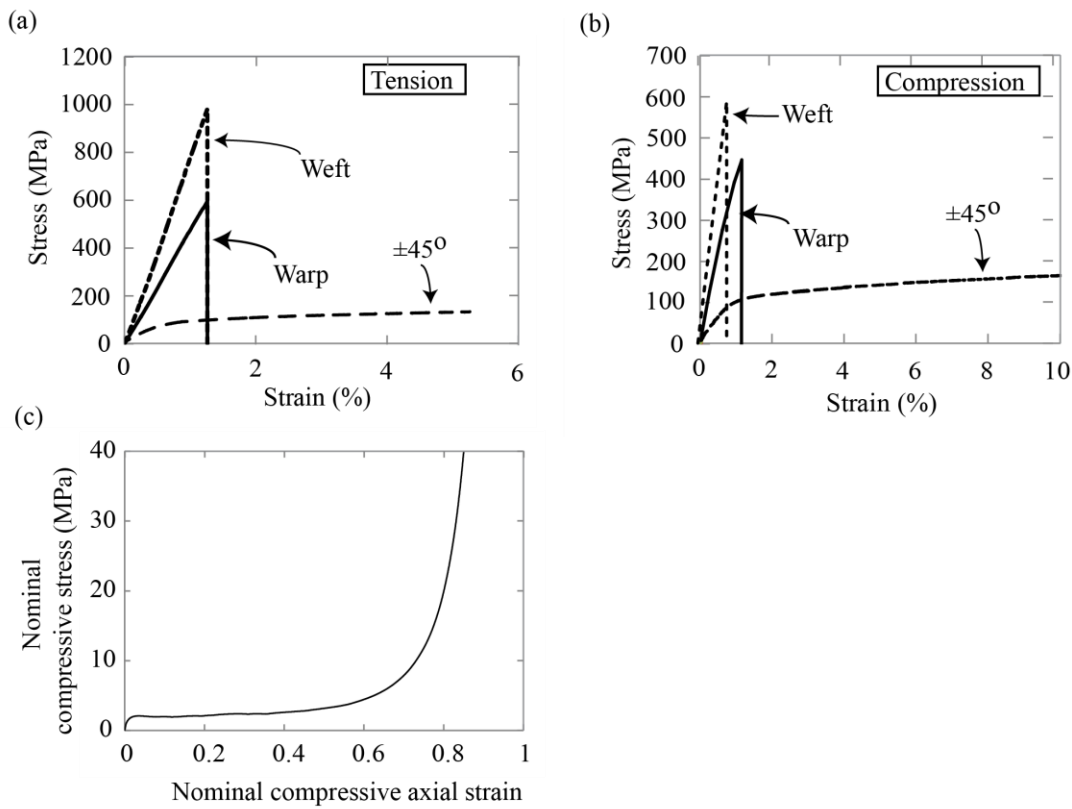
838　Figure 2. Quasi-static stress strain relationships for 3D woven carbon composite material for (a) tension and

839　(b) compression. (c) Quasi-static uniaxial compression stress-strain curve for the Alporas aluminium foam

840　projectile.

841
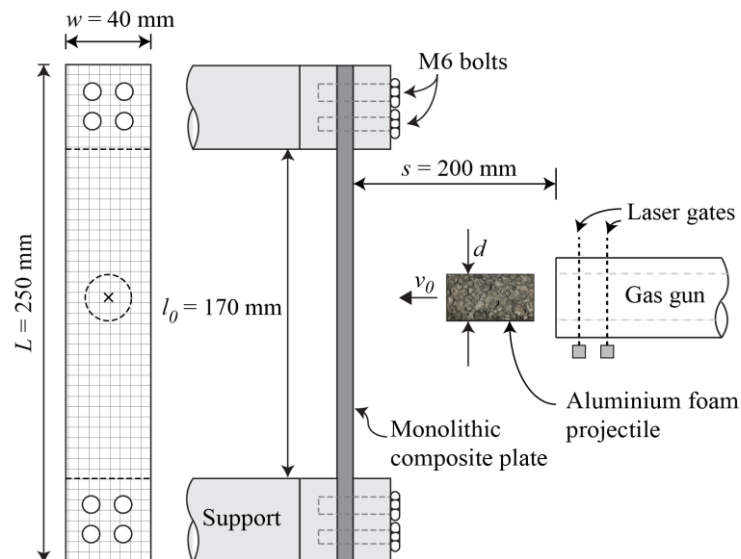
842   Figure 3 Sketch of experimental set up of dynamic soft impact tests on orthogonal 3D woven composite

843   panels.
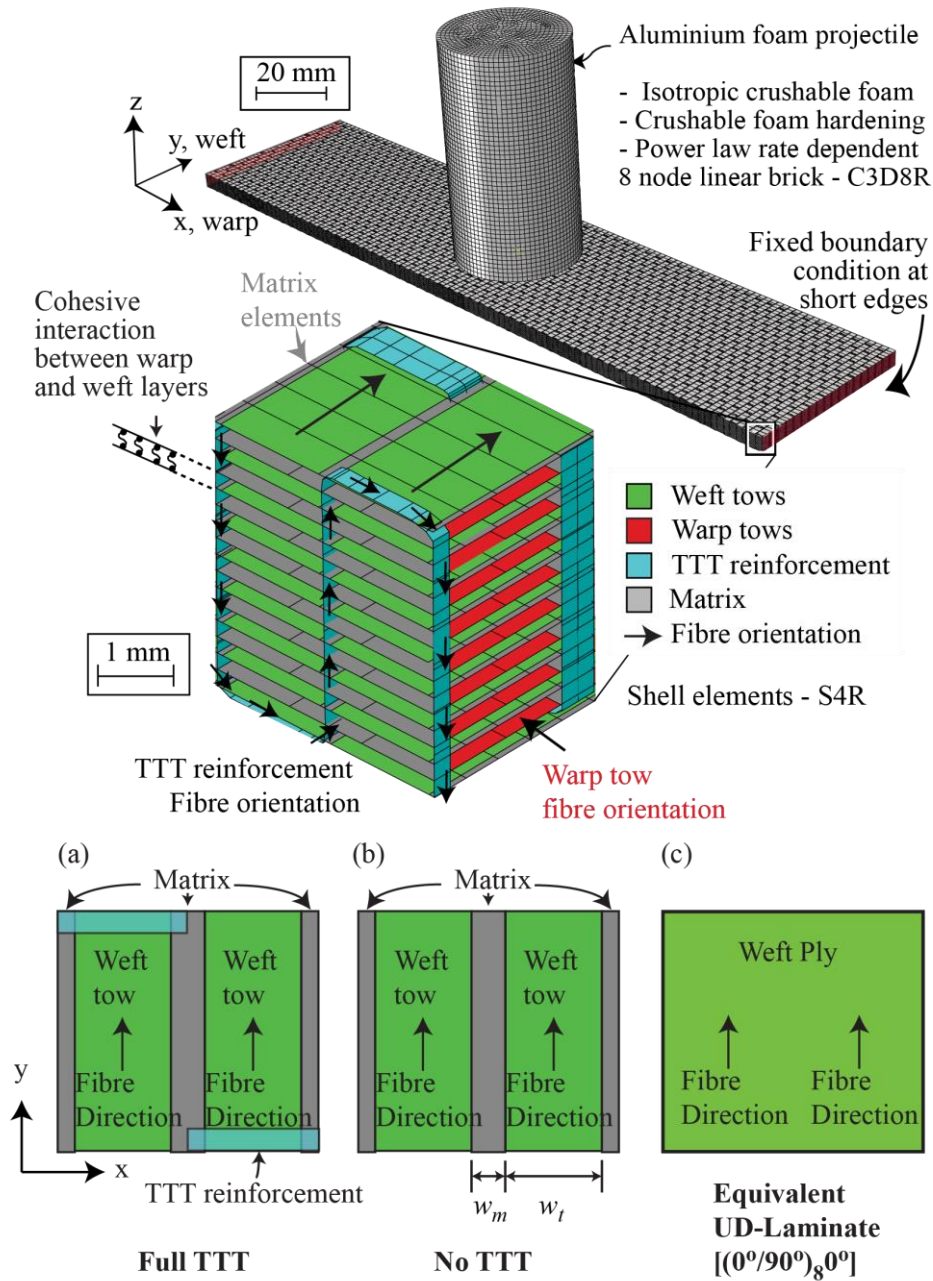
844

845   Figure 4. Finite element model for the simulation of orthogonal 3D woven carbon composite beam samples

846   undergoing soft impact, with beam orientated along the x-direction (warp). Arrows indicate direction of fibre

847   orientation. Sketches of top layers for (a) Full TTT (b) No TTT and (c) Equivalent UD-Laminate models are

848   also shown. (For interpretation of the colour legend in this figure, the reader is referred to the web version of

849   this article.)
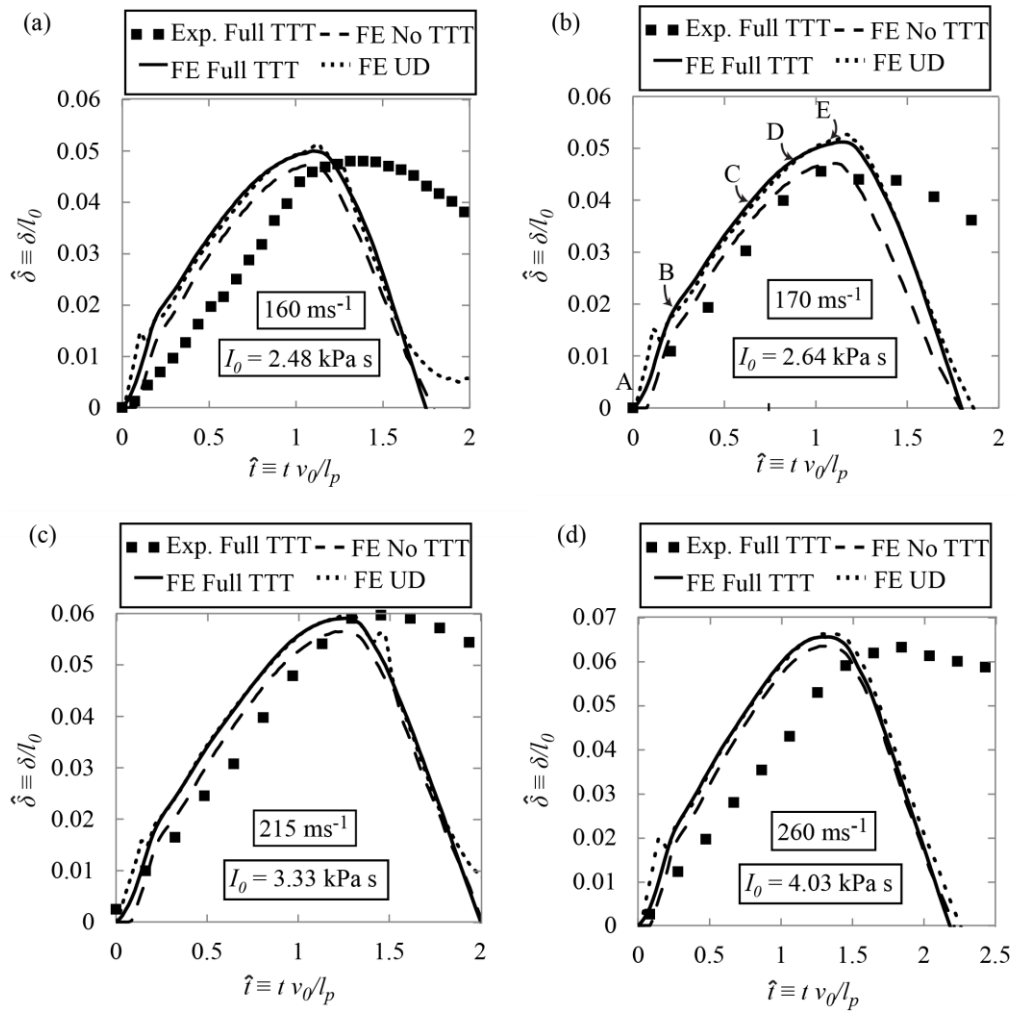
Figure 5. Comparison of experimental results for Full TTT material and FE prediction for normalised back-face deflection $\hat{\delta} \equiv \delta / l_0$ as a function of normalised time $\hat{t} \equiv t\, v_0 / l_p$. Full TTT beams orientated along the y-direction (weft). Three different case studies for numerical modelling results are presented; Full TTT reinforcement, No TTT, and an Equivalent UD-laminate material. Projectile impulses I_0 were (a) 2.5 kPa s, (b) 2.6 kPa s, (c) 3.3 kPa s, and (d) 4.0 kPa s. Points A-E corresponds to the montage images presented in Figure 6.

(a) Carbon fibre 3D woven Full TTT weft direction

(b) Carbon fibre 3D woven Full TTT weft direction - FE prediction
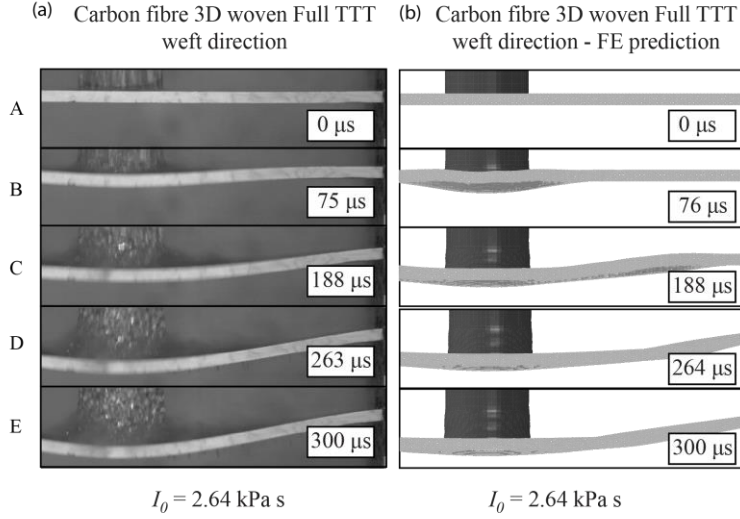
$I_0 = 2.64$ kPa s

Figure 6. Deformation montage of 3D orthogonal woven carbon-fibre composites under soft impact of impulse $I_0 = 2.64$ kPa s beams orientated along the y-direction (weft) (a) Experiment (b) Finite element prediction. Points A-E refer to the corresponding positions on Figure 5(b).
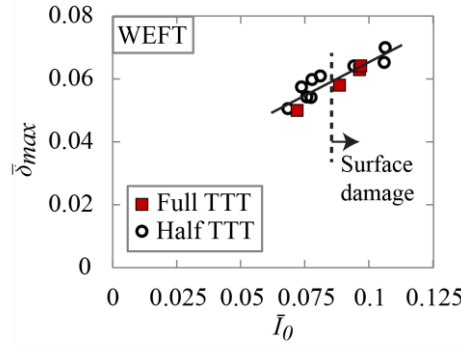
Figure 7 Comparison of the normalised maximum back face deflection $\bar{\delta}_{max}$ during soft impact as a function of normalised impact impulse $\bar{I}_0$ upon 3D woven carbon composites of two different TTT reinforcement densities.

865
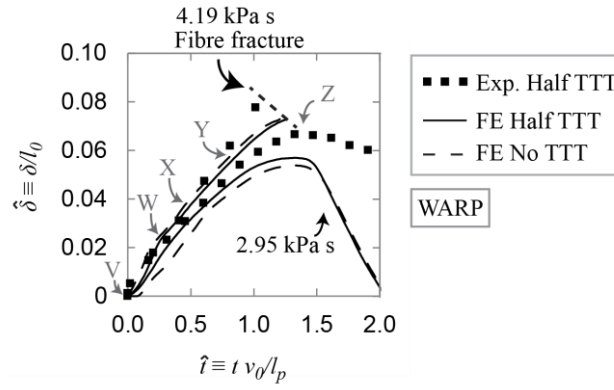
866   Figure 8. Maximum normalised back-face deflection $\hat{\delta} \equiv \delta / l_0$ against normalised time after impact

867    $\hat{t} \equiv t v_0 / l_p$. FE simulation and experimental results for beams orientated along the x-direction (warp). Points

868   V-Z correspond to the montage images presented in Figure 9.

869
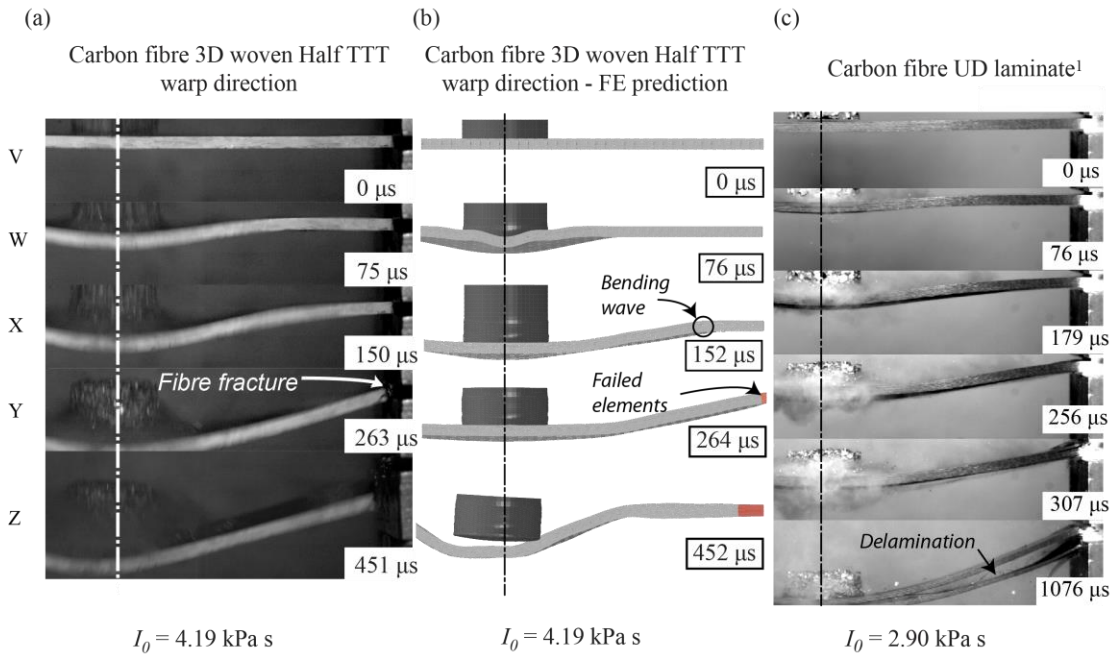
870   Figure 9. Deformation montage of carbon-fibre composites under soft impact testing showing (a) Half TTT

871   3D orthogonal woven composite beam orientated along the x-direction (warp) $I_0 = 4.19 \text{ kPa s}$, (b) Finite

872   element prediction of Half TTT 3D orthogonal woven composite beam orientated along the x-direction (warp)

873    $I_0 = 4.19 \text{ kPa s}$, and (c) UD-laminate material presented in Kandan et al. [10][1] $I_0 = 2.90 \text{ kPa s}$. Points V-Z

874   correspond to the locations noted in Figure 8.
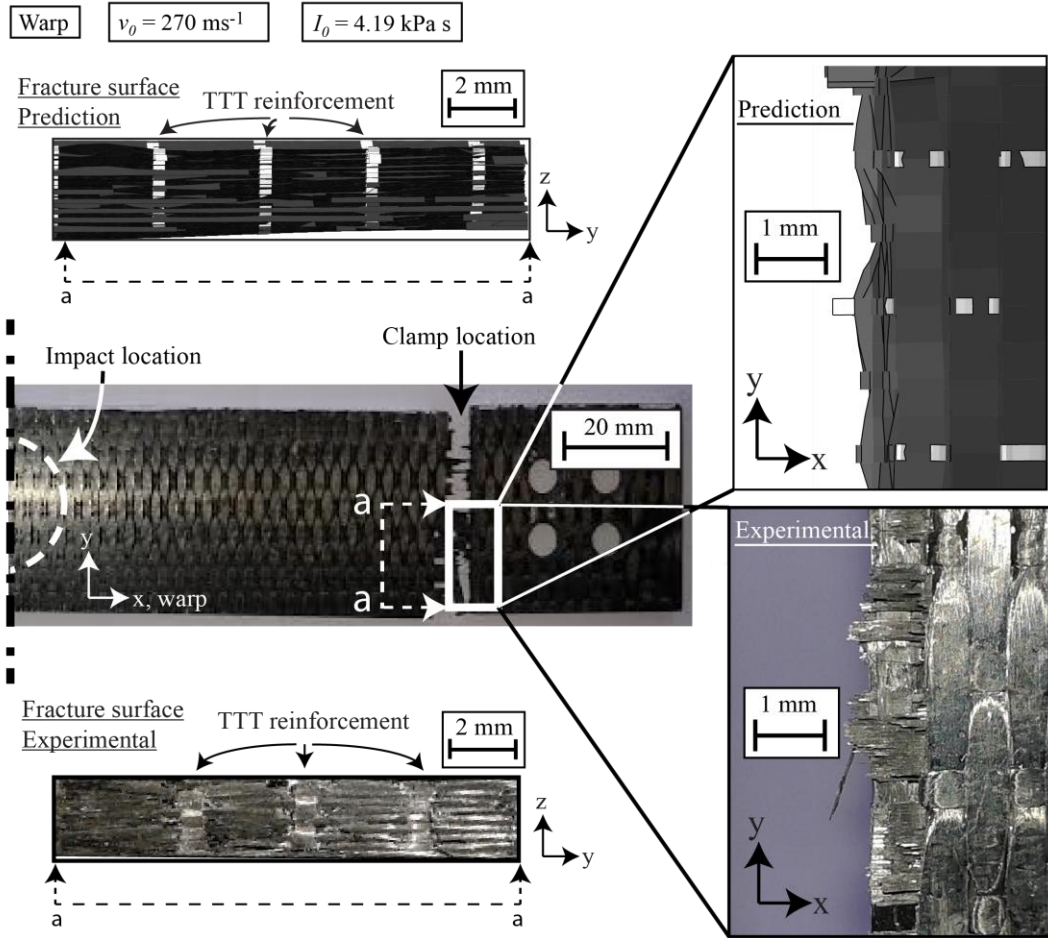
Figure 10. Photographic images and FE predictions of damage modes exhibited by Half TTT 3D woven carbon composite undergoing soft impact, tested at $I_0 = 4.19$ kPa s . Beam orientated along the x-direction (warp).
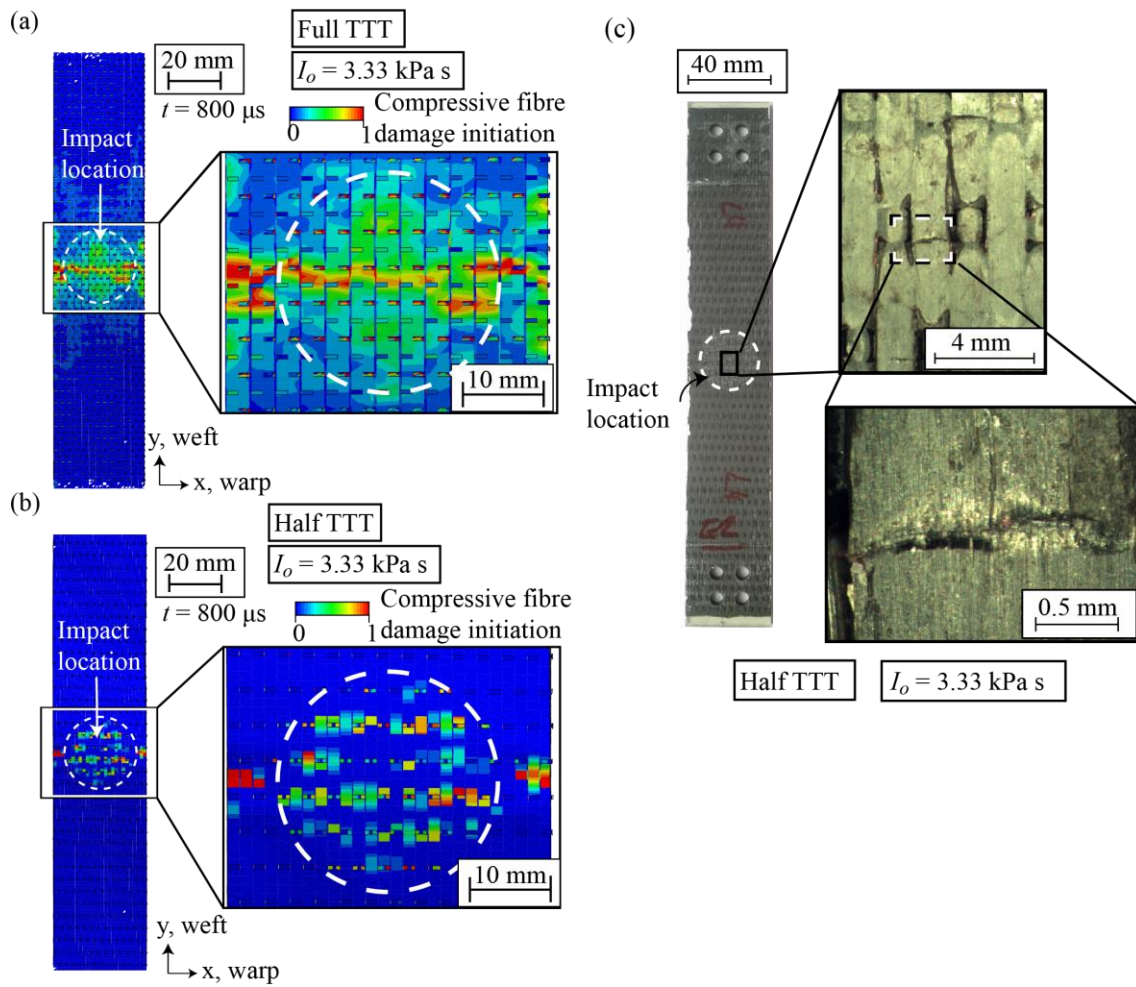
Figure 11. (a) and (b) Finite element simulations of the predicted compressive damage initiation on the front surface of orthogonal 3D woven composite beams undergoing a soft impact event $I_0 = 3.33$ kPa s for Full TTT and Half TTT material, respectively. Time t is the time after moment of projectile impact upon beam. A value of 1 corresponds to the onset of compressive fibre damage. (c) Optical microscopic images of fibre breakage on the front surface of impact tests of a Half TTT orthogonal 3D woven material after experimental impact of impulse $I_0 = 3.33$ KPa s. Beams orientated along the y-direction (weft). (For interpretation of the colour legend in this figure, the reader is referred to the web version of this article.)
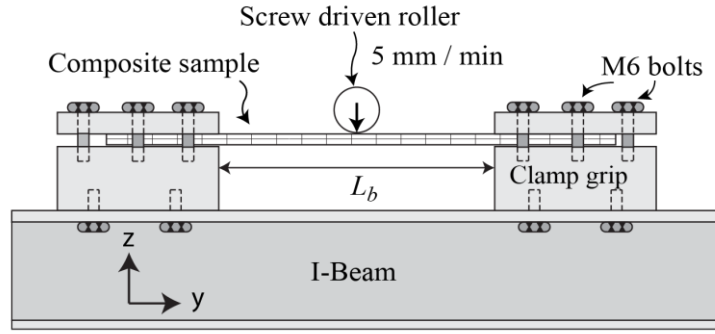
887

888   Figure 12 Sketch showing the experimental setup of the clamped beam quasi-static bending test.
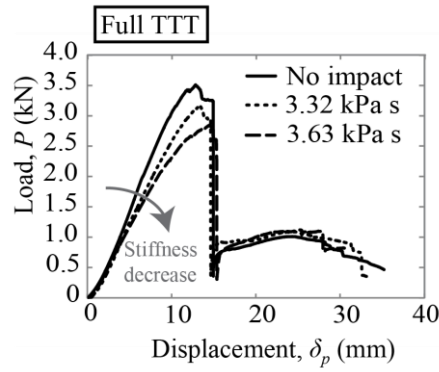

889

890   Figure 13 Load imposed by the roller P against roller vertical displacement δ_p for post-impact clamped-
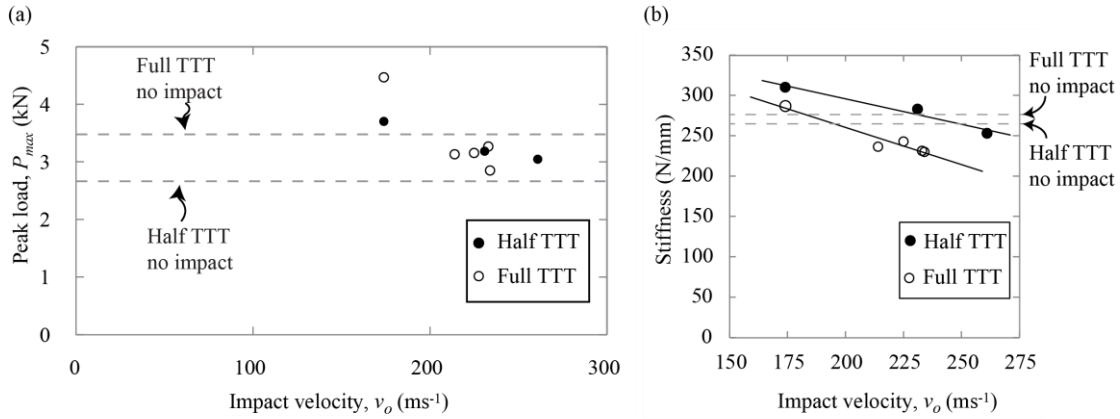891   clamped beam tests for Full TTT material. Beams orientated along y-direction (weft).

892

893   Figure 14 (a) Summary of the peak load during post-impact clamped beam testing verses the velocity of
894   impact v_0. (b) Stiffness of post-impact clamped beam testing versus the velocity of impact, v_0.
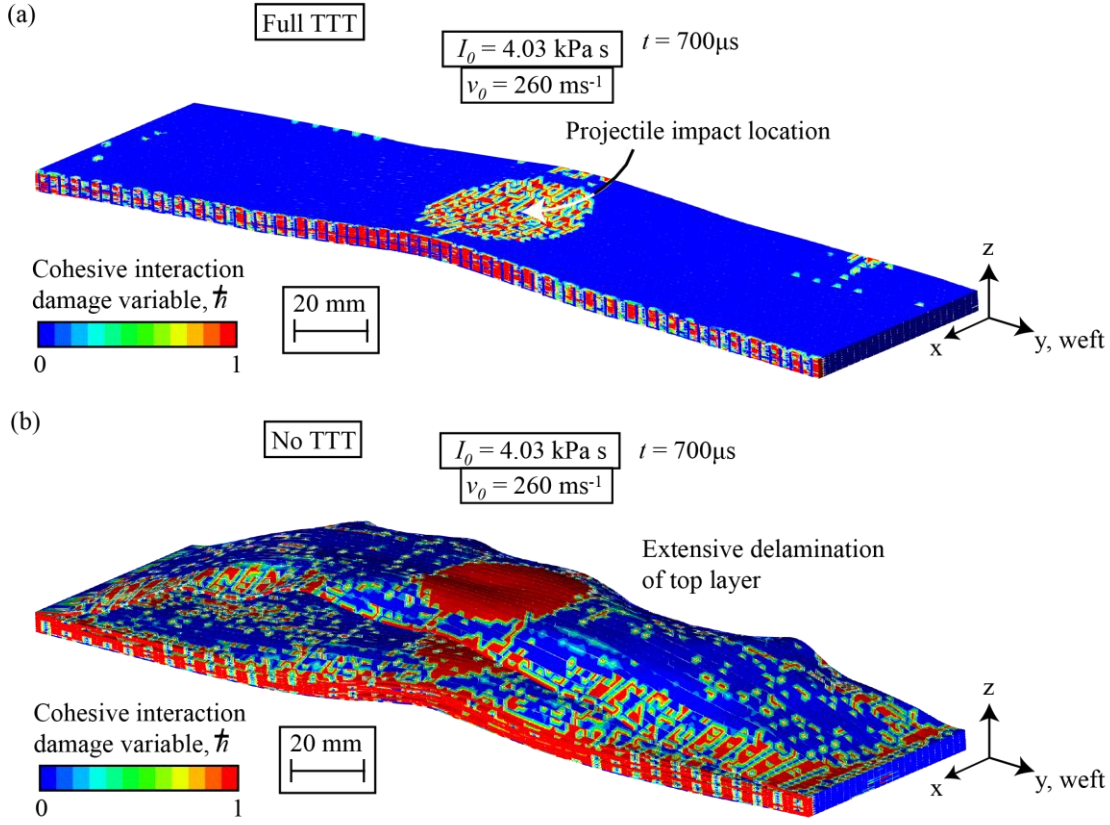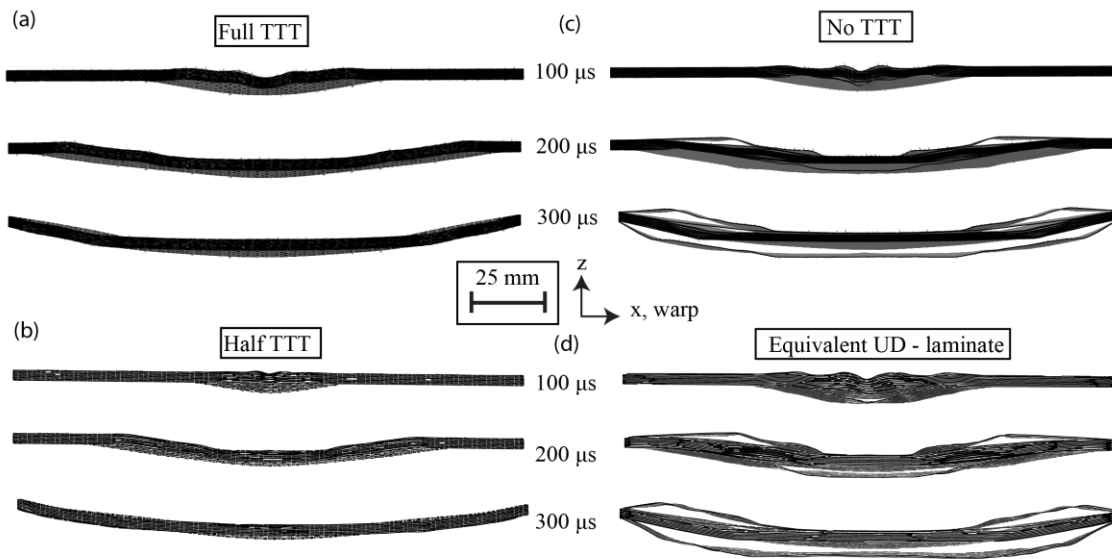
43

Figure 15. Finite element predicted deformation of an orthogonal 3D woven carbon composite undergoing a soft impact event $I_0 = 4.03 \text{ kPa s}$ showing (a) Full TTT and (b) No TTT model. Contour plot shows damage variable of cohesive interaction, $\hbar$, demonstrating locations of delamination within the beam. A value of $\hbar = 1$ indicates fully delaminated regions. $t = 0$ corresponds to the moment of projectile impact on the sample. Beams orientated along the y-direction (weft). (For interpretation of the colour legend in this figure, the reader is referred to the web version of this article.)

(a) Full TTT
(c) No TTT

100 μs
200 μs
300 μs

25 mm
z
x, warp

(b) Half TTT
(d) Equivalent UD - laminate

100 μs
200 μs
300 μs

902

Figure 16. Montage of finite element simulations of a soft impact event of impulse $I_0 = 2.96$ kPa s with cohesive contact removed on (a) Full TTT orthogonal 3D woven composite (b) Half TTT orthogonal 3D woven composite (c) 3D woven composite with TTT-reinforcement removed, and (d) Equivalent UD-laminate material. $t = 0$ corresponds to the moment of projectile impact upon the beam. Beams orientated along the x-direction (warp).